A&A 467, 955–969 (2007)
DOI: 10.1051/0004-6361:20066117

Astronomy & Astrophysics

Highly-excited CO emission in APM 08279+5255 at $z = 3.9$

A. Weiß[1], D. Downes[2], R. Neri[2], F. Walter[3], C. Henkel[1], D. J. Wilner[4], J. Wagg[4,5], and T. Wiklind[6]

[1] MPIfR, Auf dem Hügel 69, 53121 Bonn, Germany
e-mail: aweiss@mpifr-bonn.mpg.de
[2] IRAM, Domaine Universitaire, 38406 St-Martin-d'Hères, France
[3] MPIA, Königstuhl 17, 69117 Heidelberg, Germany
[4] Harvard-Smithsonian Center for Astrophysics, Cambridge, MA, 02138, USA
[5] Instituto Nacional de Astrofisica, Óptica y Electrónica (INAOE), Aptdo. Postal 51 y 216, Puebla, Mexico
[6] ESA-Space Telescope Division, STScI, 3700 San Martin Drive, Baltimore, MD 21218, USA

Received 26 July 2006 / Accepted 19 February 2007

ABSTRACT

We report the detection of the CO 4–3, 6–5, 9–8, 10–9, and 11–10 lines in the Broad Absorption Line quasar APM 08279+5255 at $z = 3.9$ using the IRAM 30 m telescope. We also present IRAM PdBI high spatial resolution observations of the CO 4–3 and 9–8 lines, and of the 1.4 mm dust radiation as well as an improved spectrum of the HCN(5–4) line. Unlike CO in other QSO host galaxies, the CO line SED of APM 08279+5255 rises up to the CO(10–9) transition. The line fluxes in the CO ladder and the dust continuum fluxes are best fit by a two component model, a "cold" component at ~65 K with a high density of $n(H_2) = 1 \times 10^5$ cm^{-3}, and a "warm", ~220 K component with a density of 1×10^4 cm^{-3}. We show that IR pumping via the 14 μm bending mode of HCN is the most likely channel for the HCN excitation. From our models we find, that the CO(1–0) emission is dominated by the *dense* gas component which implies that the CO conversion factor is higher than usually assumed for high-z galaxies with $\alpha \approx 5\,M_\odot$ (K km s^{-1} pc^2)$^{-1}$. Using brightness temperature arguments, the results from our high-resolution mapping, and lens models from the literature, we argue that the molecular lines and the dust continuum emission arise from a very compact ($r \approx 100-300$ pc), highly gravitationally magnified ($m = 60-110$) region surrounding the central AGN. Part of the difference relative to other high-z QSOs may therefore be due to the configuration of the gravitational lens, which gives us a high-magnification zoom right into the central 200-pc radius of APM 08279+5255 where IR pumping plays a significant role for the excitation of the molecular lines.

Key words. galaxies: formation – galaxies: high-redshift – ISM: molecules – galaxies: individual: APM 08279+5255 – cosmology: observations – galaxies: quasars: emission lines

1. Introduction

The existence of massive reservoirs of molecular gas at high redshifts has now been established in quasars, submillimeter galaxies and radio galaxies out to the highest redshifts (see review by Solomon & Vanden Bout 2005, and references therein). It is now of interest to study in detail the excitation conditions of the molecular gas in these high-redshift systems to search for differences of the gas properties among high-z sources and to relate them to the properties of their host galaxies. One way to do this is by studying multiple CO transitions from individual key sources (hereafter referred to as "CO line spectral energy distributions (SEDs)"). We have recently reported observations for the gravitationally lensed galaxy SMM J16359+6612 (Weiss et al. 2005a). Here we focus on new observations of one of the brightest quasars at high redshifts, the broad absorption line (BAL) quasar APM 08279+5255 at $z = 3.9$ (Irwin et al. 1998).

APM 08279+5255 has a stunning apparent luminosity of $L_{\rm bol} = 7 \times 10^{15}\,L_\odot$, one of the highest in the universe (Irwin et al. 1998). High-resolution imaging and spectroscopy by Ledoux et al. (1998) initially showed the optical source to have two images, A and B, separated by 0.″38, and showing the same spectrum, indicating that APM 08279 is gravitationally lensed. Subsequently Ibata et al. (1999) and Egami et al. (2000) found a third image, C, 0.″1 north of A, implying that this is a rare cusped lens with an odd number of images. The multiple image structure has also been seen in X-rays (Chartas et al. 2002). The lens modeling by Egami et al. (2000) indicates a high magnification factor of ~100 at optical wavelengths. The object's true bolometric luminosity would therefore be $\sim 7 \times 10^{13}\,L_\odot$, still making it one of the most luminous quasars. APM 08279 was also detected in the mm and submm dust continuum, and its SED peaks near ~30 μm (restframe), consistent with a single component dust fit with $T_{\rm dust} = 220$ K (Lewis et al. 1998) – significantly warmer than the dust emission in other high-z QSOs with typical temperatures of 50 – 80 K (see e.g. Beelen et al. 2006).

Molecular gas in APM 08279 object has been first detected through observations of the CO(4–3) and CO(9–8) lines (Downes et al. 1999; hereafter D99) using the IRAM interferometer. These high-J CO detections were followed up by observations of the CO(1–0) and CO(2–1) lines at the VLA (Papadopoulos et al. 2001; Lewis et al. 2002a). Based on the earlier observations, initial gravitational lens models suggested the CO lines arise in a compact ($r \approx 400$ pc) disk surrounding the quasar and that the CO was magnified by a factor of 5 to 20 (D99; Lewis et al. 2002a,b). Based on the morphology of the low-J CO transitions Papadopoulos et al. (2001) suggested the presence of extended molecular gas emission in this source. Subsequent GBT observations by Riechers et al. 2006 and sensitive new high-resolution VLA imaging (Riechers et al. in prep.), however, do not show evidence for such a resolved molecular gas component: the CO emission appears to be co-spatial to the emission seen in the NIR.

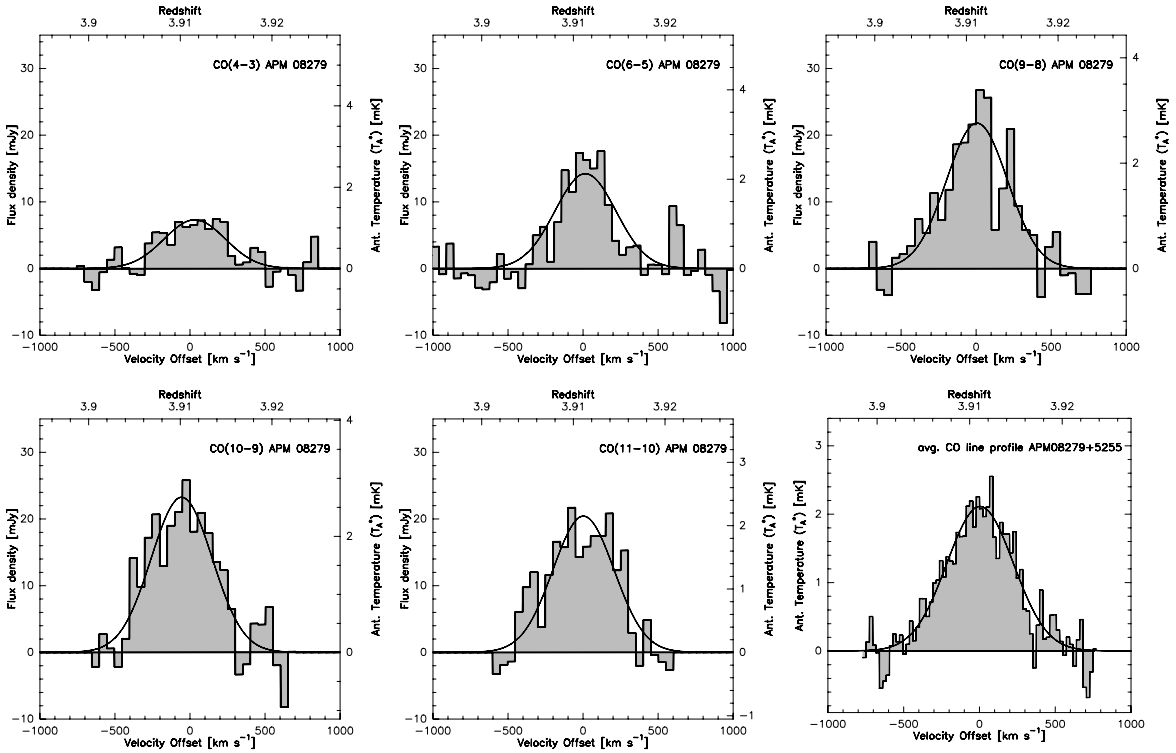

Fig. 1. IRAM 30 m telescope spectra of CO 4–3, 6–5, 9–8, 10–9, 11–10 and the average CO spectrum from APM 08279+5255, with Gaussian fit profiles superimposed. Velocity scales are relative to a redshift of $z = 3.911$. The velocity resolution for individual spectra is 50 km s^{-1}. For the average spectrum, the velocity resolution is 22 km s^{-1}. The individual spectra are plotted on the same scale in flux density (*left axis*).

While the size and mass (10^9 to $10^{10}\,M_\odot$) of the molecular gas toroid in APM 08279 is similar to those derived for other high-z QSOs (Solomon & Vanden Bout 2004) the mere detection of the CO(9–8) line in APM 08279 already indicates that the physical properties of its molecular gas phase are more extreme than what is found in other high-z QSOs. Another sign of these more extreme conditions is the detection of HCN(5−4) in this source, which also indicates high gas densities (Wagg et al. 2005). To better constrain the excitation of the molecular gas, we here present a detailed study of the CO line SED in this source. The observations were obtained at the IRAM 30 m telescope (CO 4–3, 6–5, 9–8, 10–9, and 11–10 lines). We also present Plateau de Bure interferometer long-baseline observations of the CO 4–3, 9–8, and 1.4 mm dust radiation that have higher resolution than the earlier Bure maps of this source (D99).

2. Observations and results

2.1. Pico Veleta

We observed APM 08279+5255 with the IRAM 30 m telescope on Pico Veleta, Spain, in the winters of 2004/05 and 2005/06, in excellent weather. We used the AB and CD receiver setups, with the A/B receivers tuned to CO(4–3) (3 mm band) and either CO(9–8) or CO(10–9) (lower 1 mm band) and the C/D receivers tuned to CO(6–5) (2 mm band) and CO(11–10) (upper 1 mm band). System temperatures were typically ≈140 K, 180 K, and 320 K (T_a^*) for the 3, 2, and 1 mm observations. We observed with a wobbler rate of 0.5 Hz and a wobbler throw of 50″ in azimuth, and frequently checked the pointing, which was stable to within 3″ in all runs. We calibrated every 12 min with standard hot/cold load absorbers, and estimate fluxes to be accurate to ±10% at 3 and 2 mm and 20% at 1 mm. Spectrometers were the 512 × 1 MHz filter banks for the 3 mm receivers, and the 256 × 4 MHz filter banks for the 1.3 mm receivers. In the data processing, we dropped all scans with distorted baselines, subtracted linear baselines from the remaining spectra, and then rebinned to a velocity resolution of 50 km s^{-1}. Table 1 summarizes the observing parameters, and Fig. 1 shows the spectra.

The most remarkable result of our CO line SED study of APM 08279 at the 30 m telescope is that we detect the CO(10−9) and the CO(11–10) lines (Fig. 1). To search for differences in the line profile between the mid-J and high-J lines of CO we averaged the CO(9–8) CO(10–9) and CO(11–10) spectra with equal weight for each line. The linewidth from this high-J CO spectrum is 500 ± 20 km s^{-1}, which agrees with the value derived from CO(4–3) alone (480 ± 35 km s^{-1}; D99). From the average profile of all CO lines (Fig. 1), we derive a CO linewidth of 500 ± 26 km s^{-1} and a CO redshift of $z = 3.9112 \pm 0.0004$. Our new 30 m CO(4–3) line intensity agrees with both the earlier (D99) and our new PdBI measurement. The 30 m CO(9–8) line intensity also agrees well with our new PdBI observations. Both new measurements yield a flux density slightly higher, but consistent, within the calibration error, with the previous measurements (D99).

2.2. Plateau de Bure

2.2.1. CO observations

We also observed the CO(4–3) and CO(9–8) lines with the IRAM Plateau de Bure interferometer in the long–baseline A and B configurations. The resulting data have an equivalent 6-antenna on-source integration time of 15 h, with baselines from 24 to 410 m, giving naturally-weighted synthesized beams of 1.″7 × 1.″6 at 3.2 mm and 0.″85 × 0.″71 at 1.4 mm. Receiver temperatures were 45 to 65 K at both wavelengths. The spectral correlators covered 910 km s^{-1} at 3.2 mm and 760 km s^{-1}

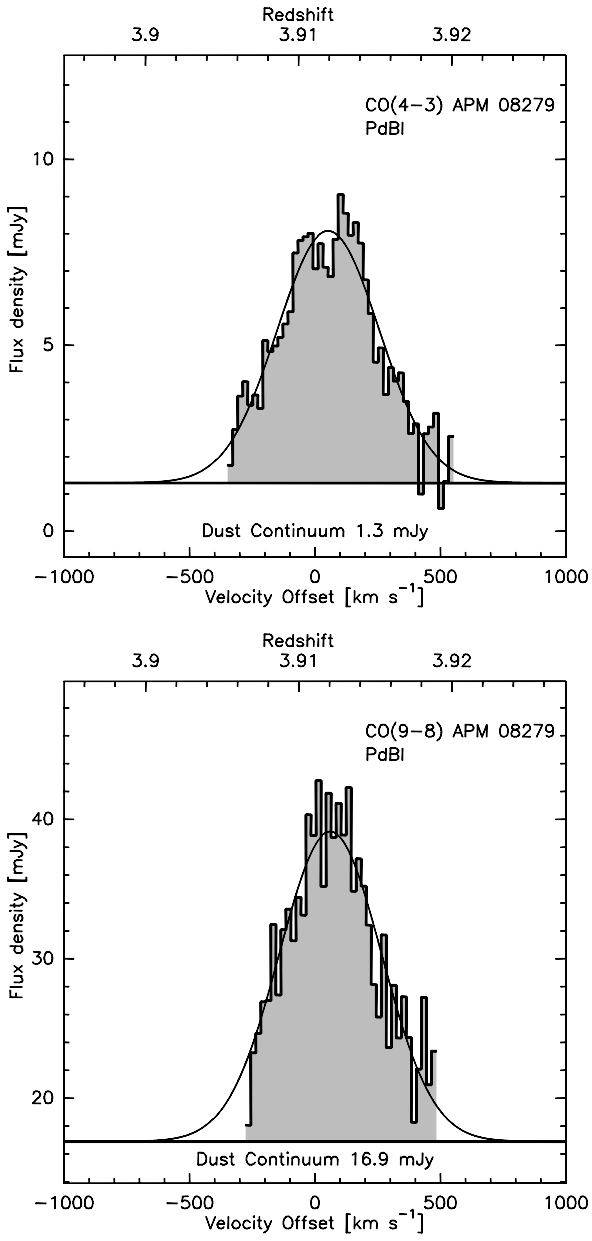

Fig. 2. Integrated CO(4–3) and CO(9–8) spectra from APM 08279+5255 obtained with the IRAM Interferometer. For both spectra the velocity offsets are given relative to a redshift of $z = 3.911$. *Upper panel*: CO(4–3) profile above the dust continuum of 1.3 mJy. The channel width is 20 km s^{-1}with an rms noise of 0.7 mJy. *Lower panel*: CO(9–8) profile above the dust continuum. The channel width is 20 km s^{-1} with an rms noise of 1.7 mJy. The dust continuum is 16.9 mJy.

at 1.4 mm, with resolutions of 8.0 and 3.6 km s^{-1} respectively. Amplitudes were calibrated with 3C84, 3C454.3, 3C273, and MWC349, and phases were calibrated with IAP 0749+540 and IAP 0804+499.

To obtain high signal-to-noise spectra, we add the older short-baseline configuration *D* data from D99 to the long-baseline data. These combined data have equivalent 6-antenna integration times of 26 h at 3.2 mm and 23 h at 1.4 mm and naturally-weighted synthesized beams of $2\farcs9 \times 2\farcs4$ at 3.2 mm and $1\farcs4 \times 1\farcs0$ at 1.4 mm. The integrated CO spectra from this data cube are shown in Fig. 2. Such spectra of the total flux can be obtained by either spatially integrating over the source map, or by doing *u,v*-plane fits to the data in each channel, with the source centroid and source size fixed to $0\farcs6$ (see below). The fit then gives the zero-spacing flux (total flux) in each channel. Both methods give the same result. For comparison with the 30 m spectra, we also fit these interferometer line profiles with single Gaussians. Table 1 summarizes our results. The CO linewidth and redshift derived from the average of the two PdBI CO spectra give 475 ± 17 km s^{-1} and $z = 3.9119 \pm 0.0002$. This redshift is higher than the corresponding value derived from the average 30 m spectrum but in good agreement with the HCN redshift measured with the PdBI. We attribute these differences to the lower S/N ratio and remaining baseline instabilities in the 30 m data. The continuum fluxes at 3.2 mm and 1.4 mm are 1.3 mJy and 16.9 mJy respectively – in agreement with the earlier data (D99).

To determine the astrometry and apparent size of the dust and CO emitting region we use the uniform weighted 1 mm data which has a spatial resolution of $0\farcs71 \times 0\farcs64$. This CO(9–8) and 1.4 mm dust maps (Fig. 3) yield a source position (Table 2) that agrees within the errors with the earlier result (D99) and coincides within $0\farcs3$ with the optical quasar (revised optical position from Irwin et al. 1998), and with the non-thermal radio source detected at 1.4 GHz (Ivison 2006).

In its long-baseline *A* and *B* configurations, the IRAM Interferometer starts to resolve the source as the peak flux is no longer equal to the total flux. But the beam size is still too large to show whether the mm-source is in three images, as in the visible and near-IR (Ibata et al. 1999; Egami et al. 2000; or in a section of an Einstein ring Lewis et al. 2002a). We estimate an overall apparent size of the CO emission region from *u, v*-plane fits to the CO(9–8) data. A one-component elliptical Gaussian fit yields an equivalent single-component CO size of $0\farcs6 \pm 0\farcs2$ (Fig. 4).

2.2.2. HCN observations

The first detection of the HCN(5–4) transition in APM 08279 was recently reported by Wagg et al. (2005). To better constrain the line parameters, in particular the line shape, we re-observed the HCN(5–4) line with the IRAM Interferometer's *D* configuration in summer and autumn 2005, and also detected the HCN line in this new, independent data set, which more than doubles the previous on-source integration time. Our final spectrum (Fig. 5) shows the combination of our new observations with the data published by Wagg et al. (2005), with the signal-to-noise ratio improved by a factor of 1.4. The Gaussian fit shown in Fig. 5 yields a HCN(5–4) peak flux density of 2.0 ± 0.2 mJy, a velocity centroid of +62 ± 15 km s^{-1} relative to our tuning redshift of $z = 3.911$ (90.229 GHz), and an integrated HCN flux density of 0.85 ± 0.10 Jy km s^{-1}, all in good agreement with the values found by Wagg et al. The dust continuum flux at this frequency is 1.3 ± 0.13 mJy. The measured HCN(5–4) linewidth of 402 ± 40 km s^{-1} is 15% more narrow than the CO linewidth. This may indicate that the HCN(5–4) line samples a slightly different region than the CO lines.The difference of the linewidth, however, has only a low significance with $\Delta V_{\rm CO} - \Delta V_{\rm HCN} = 75 \pm 45$ km s^{-1}.

3. Analysis

3.1. The dust continuum

We use our new continuum measurements together with data between 3 mm and 60 μm (restframe 700–14 μm) from the

Table 1. Line measurements in APM 08279+5255.

Spectral line:	– CO(4–3) –		CO(6–5)	– CO(9–8) –		CO(10–9)	CO(11–10)	HCN(5–4)
Rest freq. (GHz)	461.0408		691.4730	1036.9120		1151.9850	1267.0145	443.1162
Observing parameters:								
Telescope	30 m	PdBI	30 m	30 m	PdBI	30 m	30 m	PdBI
Observing freq. (GHz)	93.879	93.867	140.801	211.141	211.088	234.573	257.995	90.229
Beam FWHP (arcsec)	25	1.7×1.6	18	11	0.85×0.71	10.5	9.5	7.2×5.4
S/T_a^* (Jy/K)	6.1	–	6.7	7.9	–	8.7	9.5	–
T_{mb}/S (K/Jy)	0.22	47.8	0.19	0.23	38.1	0.20	0.20	2.90
Channel width (MHz)	1	2.5	4	4	2.5	4	4	15
Observing time (hr)	7.9	26	3.0	5.2	22.8	4.8	16.7	27.9
rms noise in 50 km s^{-1}:								
1σ in T_a^* (mK)	0.3	–	0.5	0.6	–	0.5	0.4	–
1σ in S (mJy)	1.9	0.56	3.1	4.9	1.3	4.0	4.1	0.47
Measured line parameters:								
Line center (GHz)	93.869	93.864	140.794	211.137	211.100	234.616	257.993	90.210
Redshift, z	3.9115	3.9118	3.9113	3.9111	3.9119	3.9110	3.9110	3.9121
Redshift error	±0.001	±0.0003	±0.0008	±0.0006	±0.0003	±0.0015	±0.0015	±0.0004
Line peak (T_a^*, mK)	1.2	–	2.1	2.8	–	2.7	2.2	–
Line peak (mJy)	7.3	7.5	14.3	21.9	24.2	23.3	20.5	2.0
Integ. flux (Jy km s^{-1})	3.7	3.8	7.3	11.1	12.5	11.9	10.4	0.85
Line *FWHM* (km s^{-1})	490 ± 60	470 ± 17	445 ± 40	480 ± 40	460 ± 22	480 ± 90	520 ± 50	400 ± 40
Apparent line luminosities (uncorrected for lensing):								
L'_{line} (10^{10} L_l)	14.7	15.1	12.7	8.7	9.8	7.5	5.4	3.6
L_{line} (10^9 $L_\odot$)	0.46	0.47	1.3	3.1	3.5	3.7	3.5	0.10

Errors in flux and luminosity are ±10% for CO(4–3) and (6–5), and ±20% for the other lines.
Line luminosity unit L_l = K km s^{-1} pc^2.
Luminosities are for $H_0 = 71$ km s^{-1} Mpc^{-1}, $\Omega_\Lambda = 0.73$ and $\Omega_m = 0.27$ (Spergel et al. 2003), so at $z = 3.91$, angular diameter distance $D_A = 1.474$ Gpc, or 7147 pc/arcsec, and luminosity distance $D_L = 35.556$ Gpc.

Table 2. Positions, sizes, and continuum flux densities.

Data	RA 08^h31^m (J2000)	Dec $52°45'$ (J2000)	Major axis (arcsec)	Minor axis (arcsec)	PA (deg.)	Continuum flux density (mJy)	Refs.
1.4 mm measurements:							
1.4 mm usb (dust)	$41\overset{s}{.}701$	$17\overset{''}{.}51$	$0\overset{''}{.}57 \pm 0\overset{''}{.}05$	$0\overset{''}{.}48 \pm 0\overset{''}{.}06$	54° ± 25°	16.9 ± 2.5	1
1.4 mm lsb (CO98+dust)	$41\overset{s}{.}702$	$17\overset{''}{.}49$	$0\overset{''}{.}61 \pm 0\overset{''}{.}03$	$0\overset{''}{.}55 \pm 0\overset{''}{.}03$	−14° ± 19°	—	1
CO(9–8) alone	$41\overset{s}{.}700$	$17\overset{''}{.}49$	$0\overset{''}{.}72 \pm 0\overset{''}{.}08$	$0\overset{''}{.}60 \pm 0\overset{''}{.}08$	−25° ± 28°	—	1
3.2 mm measurements:							
CO(4–3)	$41\overset{s}{.}693$	$17\overset{''}{.}63$	$0\overset{''}{.}89 \pm 0\overset{''}{.}1$	$0\overset{''}{.}43 \pm 0\overset{''}{.}1$	11° ± 10°	1.3 ± 0.2	1
HCN(5–4)	$41\overset{s}{.}680$	$17\overset{''}{.}75$	—	—	—	1.3 ± 0.2	2
Optical and cm-wave measurements:							
Optical astrometry:	$41\overset{s}{.}68$	$17\overset{''}{.}1$	—	—	—	—	3
HST NICMOS A image:	$41\overset{s}{.}64$	$17\overset{''}{.}5$	—	—	—	—	4
VLA–90 cm						5.1 ± 0.8	5
VLA–20 cm	$41\overset{s}{.}708$	$17\overset{''}{.}44$	—	—	—	3.05 ± 0.07	5
VLA–3.6 cm	$41\overset{s}{.}70$	$17\overset{''}{.}5$	—	—	—	0.45 ± 0.03	4
VLA–1.3 cm	$41\overset{s}{.}70$	$17\overset{''}{.}5$	—	—	—	0.41 ± 0.09	6

References: (1) This paper; (2) Wagg et al. (2005) and this paper; (3) Irwin et al. (1998) and private comm.; (4) Ibata et al. (1999); (5) Ivison (2006); (6) Lewis et al. (2002).
Estimated astrometric errors in the 1.4 and 3.2 mm positions are $\pm 0.01^s$ in RA and $\pm 0\overset{''}{.}1$ in Dec.

literature (for references see caption of Fig. 6) to analyze the dust temperature and the size of the dust emission region. Because the dust emission in ULIRGs becomes optically thick at a rest wavelength of ~100 μm (Downes et al. 1993) we did not use the optically thin approximation, but

$$S_\nu = \left(B_\nu(T_{dust}) - B_\nu(T_{BG})\right)\frac{(1-e^{-\tau_\nu})}{(z+1)^3}\Omega_{app}\ , \quad (1)$$

where B_ν is the Planck function. Note that since S_ν is the *observed* (amplified) flux density, the lens magnification, m, is hidden in the apparent solid angle, Ω_{app}. The dust optical depth, however, is a property of the source itself, and is independent of the gravitational lensing:

$$\tau_\nu = \kappa_d(\nu_r)\, M_{dust,\,app}/(D_A^2\,\Omega_{app}), \quad (2)$$

where κ_d the dust absorption coefficient, $M_{dust,app}$ the apparent dust mass, and D_A is the angular diameter distance to the source (here the magnification cancels out via $M_{dust,\,app}/\Omega_{app}$).

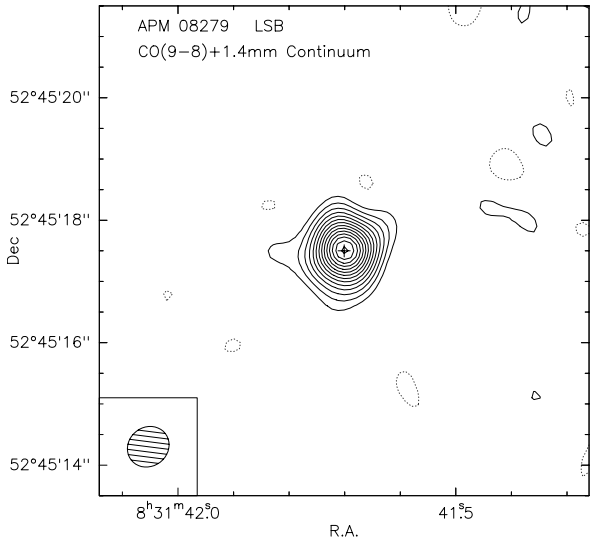

Fig. 3. Map of an 8″ field around APM 08279 made with the IRAM Interferometer at 1.4 mm. The signal is the CO(9–8) line integrated over 760 km s^{-1}, plus the 1.4 mm dust emission at the highest spatial resolution (uniform weighting, beam: 0.″71×0.″64 (*lower left inset*)). Contours start at 3σ = 1.35 mJy beam^{-1} and increase in steps of 3σ. The peak is 19.4 mJy beam^{-1} (43σ) and the spatially-integrated flux is 33.9 mJy.

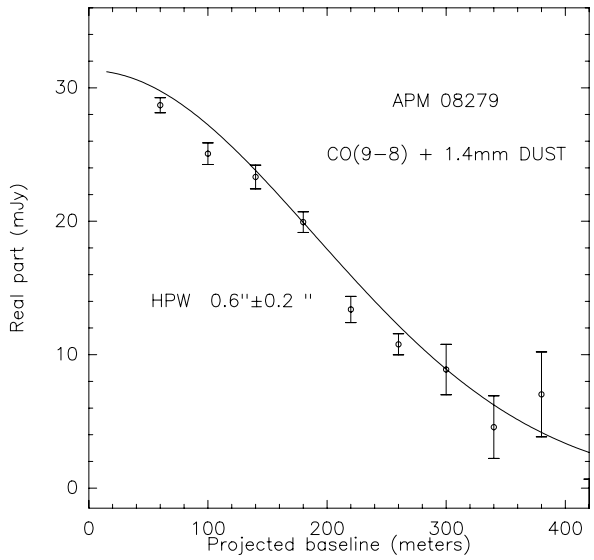

Fig. 4. Size measurement with the IRAM Interferometer: visibility amplitudes of the signal in the receivers' lower sideband at 1.4 mm. The signal is the CO(9–8) line integrated over 760 km s^{-1}, plus the 1.4 mm dust emission. The plot shows the real part of the visibility amplitude vs. the projected antenna spacing, for u, v-plane data averaged in circular bins 40 m wide, with error bars of $\pm 1\sigma$. The solid curve is a circular Gaussian fit with half-power width 0.″6 ± 0.″2.

For the frequency dependence of the dust absorption coefficient we adopt

$$\kappa_{\rm d}(\nu_{\rm r}) \;=\; 0.4\,(\nu_{\rm r}/250\,{\rm GHz})^{\beta} \qquad (3)$$

with units of cm^2 per gram of dust (Krügel & Siebenmorgen 1994), and with $\beta = 2$ (Priddey & McMahon 2001). Following our CO analysis, we substitute $\Omega_{\rm app}$ by the apparent equivalent radius r_0 so that the dust spectrum can be described by $T_{\rm dust}$, $M_{\rm dust,app}$, and r_0.

The continuum data is equally well fit with a single or 2-component dust model. The single component fit is shown

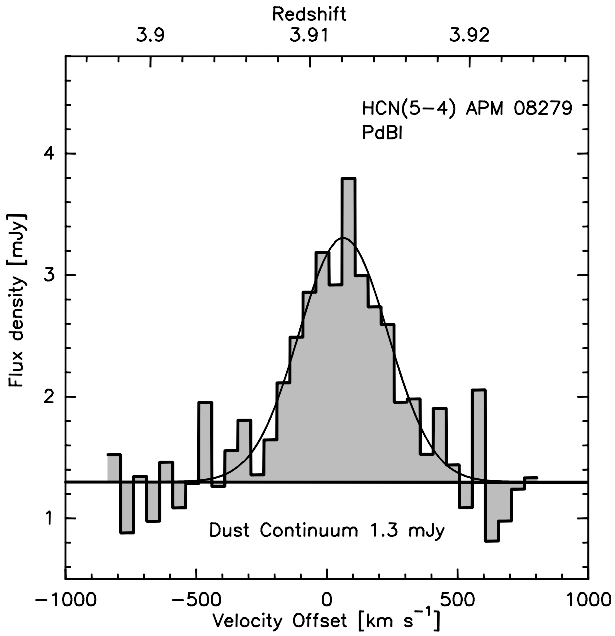

Fig. 5. HCN(5–4) spectrum from APM 08279+5255 obtained with the IRAM Interferometer. The line profile appears above the dust continuum of 1.3 mJy. The velocity scale is relative to a redshift of $z = 3.911$, the beam is 7.″2 × 5.″4 at PA 81°, and the channel width is 15 MHz (49.84 km s^{-1}). The rms noise in the spectrum is 0.47 mJy.

in Fig. 6 (left). From this fit we find $T_{\rm dust} \approx 215 \pm 10$ K, $M_{\rm dust} \approx 7.5 \times 10^8\, m^{-1}\, M_\odot$ (±10%) and $r_0 \approx 680 \pm 35$ pc. The 2-component fit is shown in Fig. 6 (right). For convenience we call these the "cold" and "warm" components. They correspond to the "starburst" and "AGN" components respectively, in similar fits to the dust spectrum by Rowan-Robinson (2000) and Beelen et al. (2006; see also the multi-component fits to APM 08279 by Blain et al. 2003). To reduce the number of free parameters, we assume that the overall size of the dust emission region is similar to that of the CO lines, and fix the equivalent (magnified) radius r_0 to 1150 pc (from the 2-component CO model). We then determine dust temperatures and masses (times magnification m) of both components, and the relative area filling factor of the warm and cold components. We fit these five free parameters to the data points above 43 GHz (upper limit only) and below the IRAS 25 μm point.

For the "cold" dust component, we find $T_{\rm cold} \approx 65 \pm 18$ K and M(cold dust) $\approx 2.6 \times 10^9\, m^{-1}\, M_\odot$ (±25%). The "warm" component has $T_{\rm warm} \approx 220 \pm 30$ K, M(warm dust) $\approx 2.1 \times 10^8\, m^{-1}\, M_\odot$ (±65%). The area filling factors we derive for the "cold" and "warm" dust components are 70 ± 10% and 30 ± 10% respectively. For the "cold" component, the dust continuum becomes opaque for rest wavelengths shorter than 300 μm ($\lambda_{\rm obs} \approx$ 1.3 mm). The implied FIR luminosity is $L_{\rm FIR} \approx 2.0 \times 10^{14}\, m^{-1}\, L_\odot$ (with $L_{\rm FIR}$ integrated from 40–120 μm restwavelength, Helou et al. 1985). The contributions from the cold and warm components are $2 \times 10^{13}\, m^{-1}\, L_\odot$ and $1.7 \times 10^{14}\, m^{-1}\, L_\odot$ respectively.

3.2. The CO line SED

The peak and velocity-integrated fluxes of the CO lines (Table 1) increase with rotational quantum number up to the 9–8 line. Beyond this transition the CO line SED flattens or even starts to decrease as for the 11–10 line. The peak of the CO line SED

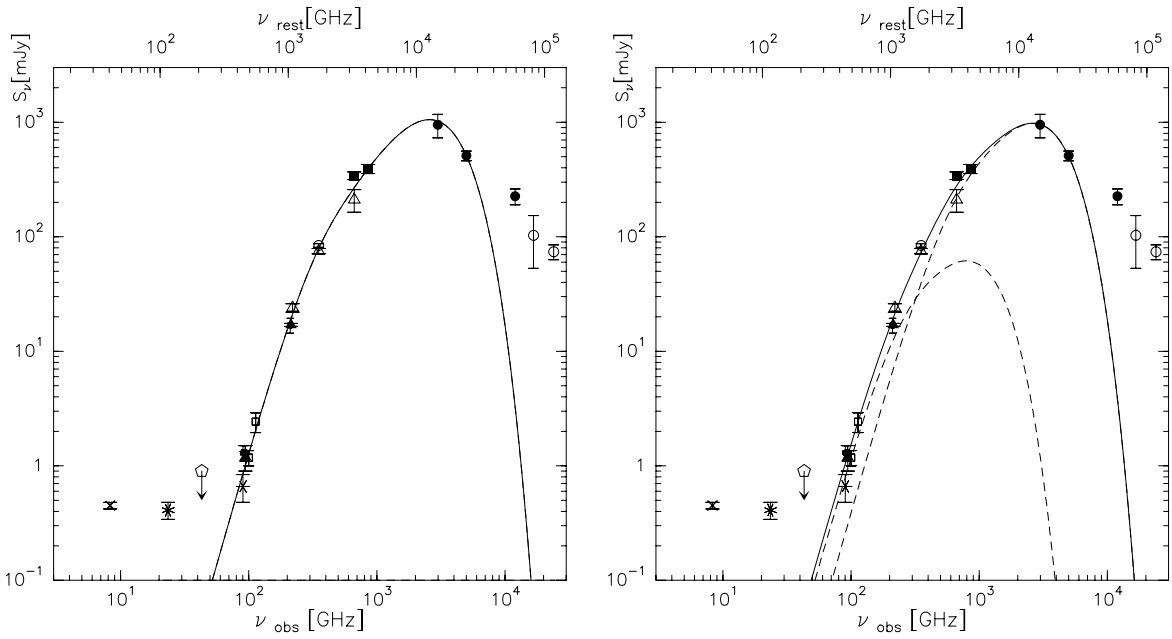

Fig. 6. Single component (*left*) and two component (*right*) dust models for APM 08279+5255. The continuum fluxes are from Irwin et al. (1998), Lewis et al. (1998, 2002a), Downes et al. (1999), Egami et al. (2000), Papadopoulos et al. (2001), Barvainis & Ivison (2002), Wagg et al. (2005), Beelen et al. (2006) and this work.

occurs at 10−9 line. The CO line luminosity, $L'_{\rm CO}$, in K km s^{-1} pc^2, is defined by

$$L'_{\rm CO} = 3.25 \times 10^7 \, S_{\rm CO}\,\Delta V \nu_{\rm obs}^{-2} \, D_L^2 \, (1+z)^{-3}, \quad (4)$$

where the integrated CO flux $S_{\rm CO}\,\Delta V$ is in Jy km s^{-1}, the observed frequency $\nu_{\rm obs}$ is in GHz, and the luminosity distance $D_{\rm L}$ is in Mpc (e.g., Solomon et al. 1997). For transitions with $J > 4$ the CO line luminosities in APM 08279 are monotonically decreasing which shows that theses lines are subthermally excited. Interestingly, the line luminosities of the CO(1–0) and CO(2–1) transitions are also lower than the line luminosity of the CO(4−3) line (Papadopoulos et al. 2001; Riechers et al. 2006), which indicates that the low-J transitions of CO have only moderate opacities.

3.2.1. CO LVG modeling

To investigate the CO excitation in more detail, we first apply a spherical, single-component, large velocity gradient (LVG) model. We use the collision rates from Flower (2001) with an H_2 ortho-to-para ratio of 3. To compare the observations with the LVG-predicted Rayleigh-Jeans brightness temperatures, $T_{\rm b}$, we convert the latter to flux densities via

$$S_{\rm CO} = \Omega_{\rm app}\, T_{\rm b}/(1+z)\, 2k\nu_{\rm obs}^2/c^2, \quad (5)$$

where $\Omega_{\rm app}$ is the apparent source solid angle (i.e., true source solid angle times gravitational magnification). Our analysis thus yields not only the gas density and temperature, but also an estimate of the magnified CO size that can be compared with the interferometer measurements. Note that $\Omega_{\rm app}$ is not a function of the rotational quantum number J for a given LVG solution. We define the equivalent source radius as

$$r_0 = D_{\rm A} \sqrt{\Omega_{\rm app}/\pi}\,, \quad (6)$$

where $D_{\rm A}$ is the angular size distance to the source, and $\Omega_{\rm app}$ is the magnified solid angle that we derive from the LVG-model brightness temperatures. This equivalent radius r_0 would be equal to the true source radius if the CO were in an unlensed, face-on, filled circular disk.

The total H_2 mass from the LVG models can be obtained using the CO emitting area (expressed as r_0) and the H_2 column density calculated via

$$N_{\rm H_2} = 3.086 \times 10^{18}\, n({\rm H_2})\, \frac{\Delta V_{\rm turb}}{{\rm d}v/{\rm d}r} \quad (7)$$

to estimate the number of H_2 molecules and therefore the gas mass. In this equation $\Delta V_{\rm turb}$ is the turbulence linewidth and ${\rm d}v/{\rm d}r$ the velocity gradient of the LVG model. Thus $\Delta V_{\rm turb}/({\rm d}v/{\rm d}r)$ is the equivalent path length through the molecular disk. The LVG gas mass is given by

$$M_{\rm LVG} = 0.21\, r_0^2\, n({\rm H_2})\, \frac{\Delta V_{\rm turb}}{{\rm d}v/{\rm d}r}\ [M_\odot]. \quad (8)$$

This LVG mass includes a correction of 1.36 to account for the mass contribution of helium. Note that $\Delta V_{\rm turb}$ in APM 08279 is not equal to the observed linewidth as the later is dominated by the rotation of the circumnuclear disk and not by its radiatively effective random motions of the gas along a line of sight.

3.2.2. Single-component LVG models for CO

We first use a CO abundance per velocity gradient of $[{\rm CO}]/({\rm d}v/{\rm d}r) = 8 \times 10^{-5}\,{\rm pc\,(km\,s^{-1})^{-1}}$. For this value, models with enough excitation to match the observed high-J fluxes, however, predict high CO opacities, even for CO(1–0), so the line luminosities are predicted to stay constant from CO(1–0) to (4–3), while the observations show a deficit in the lowest lines (Papadopoulos et al. 2001). For lower CO abundance per velocity gradient, the CO opacities are lower, because the implied CO column densities per velocity interval are reduced. For $[{\rm CO}]/({\rm d}v/{\rm d}r) = 1 \times 10^{-5}\,{\rm pc\,(km\,s^{-1})^{-1}}$, most of the LVG models that fit the high-J lines also have low enough opacities to reproduce the observed fluxes of the low-J CO lines. Thus all the

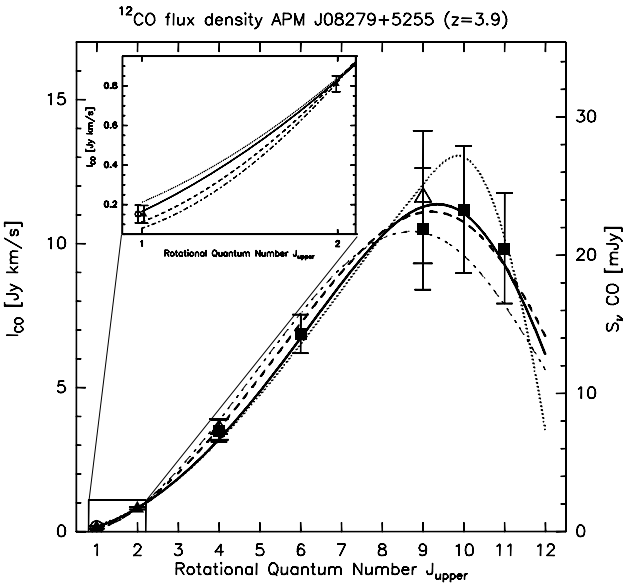

Fig. 7. Observed CO fluxes vs. rotational quantum number (CO line SED) for APM 08279+5255, obtained with the IRAM 30 m telescope (filled squares) and the IRAM Interferometer (open triangles) (D99; this paper). Errors include the calibration uncertainties. The fluxes for the 1–0 and 2–1 lines are from Papadopoulos et al. (2001, filled triangles), and Riechers et al. (2006, circle at J=1). The single-component LVG model fluxes are shown for ($n(H_2)$, T_{kin}) combinations as follows: solid line: ($10^{4.4}$ cm^{-3}, 125 K); dashed line: ($10^{4.2}$ cm^{-3}, 220 K); dotted line: ($10^{5.4}$ cm^{-3}, 40 K); dashed-dotted line: ($10^{4.0}$ cm^{-3}, 350 K). The inset shows a zoom, for the observed and model-predicted fluxes of the 1−0 and 2–1 lines. The two CO(1–0) data points are shown with a small offset in the rotational quantum number for legibility reasons.

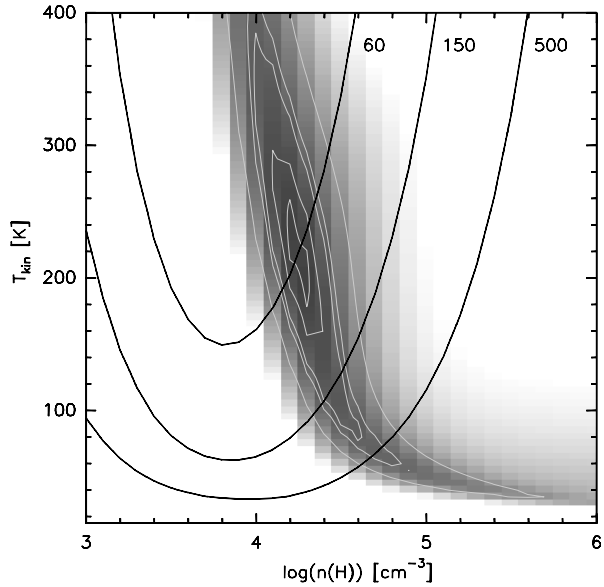

Fig. 8. χ^2 distribution for a single component LVG model fit to the observed line luminosity ratios (greyscale and grey contours, contours: χ^2 = 2, 4, 8, 10 and 20). The CO abundance per velocity gradient for the LVG models is [CO]/(dv/dr) = 1×10^{-5} pc (km s^{-1})$^{-1}$. Black lines show gas to dust mass ratios of 60, 150 and 500 calculated from the LVG H_2 mass for a dust mass of $M_{dust} = 7.5 \times 10^8\, m^{-1}\, M_\odot$ (single component dust fit, see Sect. 3.1). For the calculation of the LVG H_2 mass we have used a turbulence line width of dv_{turb} = 100 km s^{-1} and a velocity gradient of (dv/dr) = 5 km s^{-1} pc^{-1} (see also Sect. 4.2).

lines from CO(1–0) to CO(11–10) could be fit with a *single-component* LVG model. Similar low values for [CO]/(dv/dr) (i.e., a large velocity spread) in nearby starburst galaxies likely also explain the low ^{13}CO/^{12}CO ratios observed in their nuclei (e.g. Aalto et al. 1991; Paglione et al. 2001). In the following, we therefore fix [CO]/(dv/dr) to 1×10^{-5} pc (km s^{-1})$^{-1}$.

Figure 7 shows the results of fitting the observed CO fluxes with selected single-component LVG models. A good fit to the observations is provided by an H_2 density of $10^{4.4}$ cm^{-3}, a gas temperature of T_{kin} = 125 K and an equivalent (magnified) radius of r_0 = 910 pc. For these parameters, the CO(1–0) optical depth is only 1.3. The CO(2–1)/CO(1–0) line luminosity ratio is then 1.25, in agreement with the observations (Papadopoulos et al. 2001). The best fitting solution is provided by $n(H_2)$ = $10^{4.2}$ cm^{-3}, T_{kin} = 220 K and r_0 = 790 pc. Other temperature–density combinations with similar H_2 pressure also match the data (Fig. 7, Fig. 8). For H_2 densities below $10^{4.0}$ cm^{-3}, however, the model predictions fail to reproduce the observed fluxes in the high-J lines. The kinetic temperature is poorly constrained by our models. Lower-temperature models with H_2 densities greater than 10^5 cm^{-3} and $T_{kin} \sim 50$ K will also make the CO line SED turn over at the 10–9 line. For these cold, dense solutions, the turnover of the CO SED is much steeper than for the warm solutions, so in case better data were to become available, this predicted steep slope might allow us to distinguish between cold and warm gas. For the densest solutions, however, the models overestimate the 1–0 flux because the low-J opacities become too high. In Fig. 8 we show the results of a χ^2 test for the single component LVG model. In this plot we also show the resulting gas to dust mass ratio. The plot demonstrates that solutions with an H_2 density in excess of 10^5 cm^{-3} lead to very high LVG gas masses which imply unrealistically high gas to dust mass ratios (>1000). The warmest and coolest possible LVG solutions limit the equivalent (magnified) size of the emission region to the range $r_0 \approx 750-1850$ pc. Using a gas to dust mass ratio of 500 as a plausible upper limit restricts the emission region further to $r_0 \approx 750-1350$ pc.

3.2.3. Two component LVG model for CO

Similar to the dust SED we can also split the CO line SED into two components. Such a 2-component model matches the widespread view that the ISM contains dense, star-forming molecular cloud cores (traced by HCN) and more diffuse gas in the cloud envelopes (e.g. Solomon et al. 1992). In this picture, the dense HCN-emitting cores also emit CO lines, with a CO-SED extending to higher J than the CO-SED of the lower-density clouds. We therefore fit the CO-SED with a 2-component model, so that the sum of *both* CO components agrees with the observed CO SED. As the kinetic temperature for both components is expected to be similar to, or higher than the dust temperature we have used the dust temperatures to break the degeneracy between the kinetic temperature and the H_2 density. A good solution for all the observed CO lines with kinetic temperatures similar to the dust temperatures is shown in Fig. 9. This model has a high-density component with $n(H_2) \approx 10^{5.0}$ cm^{-3}, $T_{kin} \approx 65$ K, and a source equivalent (magnified) radius of $r_0 \approx 995$ pc. It also has a warmer, lower-density component with $n(H_2) \approx 10^{4.0}$ cm^{-3}, $T_{kin} \approx 220$ K, and $r_0 \approx 575$ pc.

This 2-component model does not necessarily imply that the warmer gas is closer to the AGN. The two components could just as well be randomly mixed together in a single circumnuclear disk with an equivalent (magnified) radius of $r_0 \approx 1150$ pc, with relative area filling factors of 75% and 25% for the cooler and

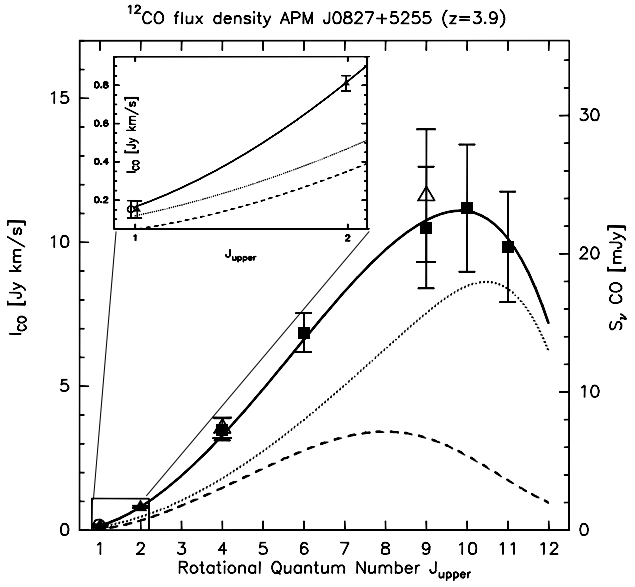

Fig. 9. 2-component model for the CO lines. The dotted line represents the "cold", dense gas, the dashed line the "warm" gas and the solid line the sum of both components. Model parameters are listed in Table 3.

warmer gas respectively – similar to the relative filling factors derived from the dust continuum. In contrast to the single component model the dense gas phase in this 2-component model only results in a gas to dust mass ratio of ∼150 as the dust mass in the cold dense component is much higher than the dust mass derived from a single component fit. Interestingly, the contribution of the cold, dense gas to the CO(1–0) line luminosity exceeds that of the warm gas phase. The (gravitationally-amplified) CO(1–0) line luminosities associated with both components are $L'_{\rm CO}(\rm cold) = 7.4 \times 10^{10}\,\rm K\,km\,s^{-1}\,pc^2$ and $L'_{\rm CO}(\rm warm) = 3.0 \times 10^{10}\,\rm K\,km\,s^{-1}\,pc^2$.

3.3. Relation to HCN

3.3.1. Collisional excitation

Our finding that the CO emission arises from high-density gas ($n(\rm H_2) > 10^4\ \rm cm^{-3}$) is supported by the detection of the HCN(5−4) line in this source (Wagg et al. 2005). In the following we use our CO single component LVG solutions to check whether the HCN(5–4) emission emerges from the same CO-emitting volume, or if we need additional gas at even higher density, as in the 2-component CO model, to explain the observations. For the LVG models of HCN, we use collision rates from Schoier et al. (2005) and assume a relative abundance ratio of [HCN/CO] = 10^{-4} (Helfer & Blitz 1997; Wang et al. 2004). This gives $[\rm HCN]/(\rm d\it v/\rm d\it r) = 1 \times 10^{-9}\,\rm pc\,(km\,s^{-1})^{-1}$. The net result is that for the single component model only the coldest, densest models ($n(\rm H_2) \approx 10^{5.4}\ \rm cm^{-3}$, $T_{\rm kin} \approx 40\,\rm K$, $r_0 \approx 1800\,\rm pc$) can excite HCN to produce the observed HCN(5–4) flux density. As noted above, these models fail to reproduce a CO(2−1)/CO(1−0) ratio larger than unity, lead to unrealistically high gas to dust mass ratios and are also inconsistent with the high dust temperatures derived for APM 08279. Conversely, warmer CO models with lower $\rm H_2$ density provide less than 15% of the observed HCN(5–4) luminosity. Hence, a single-component model cannot simultaneously explain the CO and HCN line luminosities.

Wagg et al. (2005) have argued that an increased HCN abundance may be responsible for the bright HCN emission. Their calculations suggest that a relative HCN abundance of [HCN/CO] $\approx 10^{-2}$, thus 2 orders of magnitude above the standard abundance ratio (Wang et al. 2004), is required in order explain the observed HCN and CO luminosities from a single gas component. Enhanced HCN abundances can be caused by an increased ionization rate in the vicinity of an AGN (see Wagg et al. 2005 and reference therein). Models however suggest that this increase is only modest ([HCN/CO] = 5×10^{-4}, Lepp & Dalgarno 1996). For NGC 1068 Usero et al. (2004) suggested that X-rays drive the abundances ratio to [HCN/CO] $\approx 10^{-3}$. But even if we use this increased HCN abundance, single component models with kinetic temperatures similar to the dust temperature fail to reproduce the observed HCN(5–4) flux density by a factor of 2 or more.

In the context of the 2-component model the predicted HCN(5–4) luminosity increases because the density of the cold dense gas is much higher than that derived from the one-component model. But even for this gas phase, which has a density comparable to that derived for the HCN emitting volume in local IR luminous sources (Greve et al. 2006), the predicted HCN(5–4) luminosity is much smaller than the observed value. We can, however, increase the $\rm H_2$ density of the cold gas component if kinetic temperatures below the dust temperature are considered. An equally good fit to all the observed CO lines that also matches the HCN(5–4) luminosity can be obtained using a high-density component with $n(\rm H_2) \approx 10^{5.7}\ \rm cm^{-3}$, $T_{\rm kin} \approx 45\,\rm K$, and a source equivalent (magnified) radius of $r_0 \approx 1125\,\rm pc$ as well as a warmer, lower-density component with $n(\rm H_2) \approx 10^{4.0}\ \rm cm^{-3}$, $T_{\rm kin} \approx 200\,\rm K$, and $r_0 \approx 650\,\rm pc$. The high density for the cold gas component, however, leads again to a very high gas to dust mass ratio of ∼1000. Given the high metalicity of APM 08279 (2 to 5 times solar as suggested by X-ray observations of the iron K-shell absorption edge, Hasinger et al. 2002), this makes it very unlikely that the HCN(5–4) luminosity can be explained within a pure collisional excitation scheme.

3.3.2. IR-pumping of HCN

Another potential mechanism to increase the HCN luminosity is to boost the HCN by infrared excitation, notably through the stretching and bending modes at 3, 5, and 14 μm. Various studies have addressed this issue for local IR bright galaxies and concluded that IR pumping via the 14 μm modes is not important compared to collisional excitation (e.g. Stutzki et al. 1988; Paglione et al. 1997; Gao & Solomon 2004). The dust SED of APM 08279, however, has a much higher contribution of warm dust compared to other sources studied in detail so far. Furthermore its dust temperature of ∼200 K is well beyond the minimum dust temperature of ∼110 K required for IR pumping via the 14 μm bending mode to become efficient (Carroll & Goldsmith 1981).

To investigate the effect of the increased IR field in APM 08279+5255 on the HCN excitation we include the first vibrational bending mode ($v_2 = 1$, see e.g. Thorwirth et al. 2003) in our LVG code. We neglected the vibrational ν_1 mode as its excitation requires ∼4 times higher IR temperatures (Carroll & Goldsmith 1981). For the computation we take 20 rotational levels into account which leads in total to 58 energy levels due to the *l−type doubling* of the $v_2 = 1$ mode. The IR field is described by a greybody spectrum with a frequency dependence in analogy to Eq. (3). The illumination of the dense gas by the IR field is parameterized by an IR delution factor. This filling factor represents the solid angle fraction of the gas exposed to the IR field.

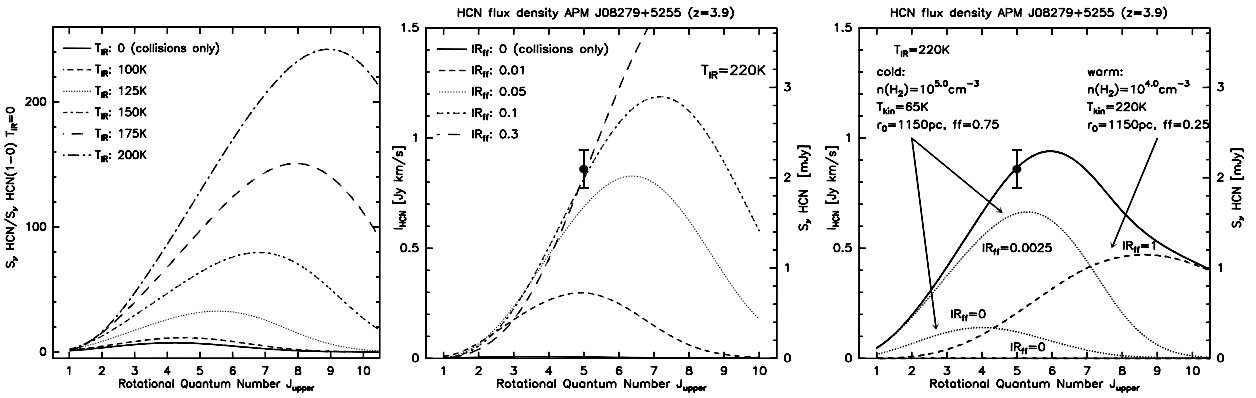

Fig. 10. *Left*: HCN line SED as a function of the IR radiation temperature for a H_2 density of 10^5 cm^{-3}, a kinetic temperature of 65 K and an delution factor for the IR radiation field of 10% for each model. All SEDs are normalized to the HCN(1–0) flux density for the pure collisional excitation model ($T_{\rm IR} = 0$ K). The plot exemplifies the large effect of IR pumping on the HCN excitation for dust temperatures above ∼100 K. *Middle*: HCN excitation in APM 08279+5255 for gas parameters as derived from the single component dust/CO model ($n(H_2) = 10^{4.2}$ cm^{-3}, $T_{\rm IR} = T_{\rm kin} = 220$ K and $r_0 = 790$ pc) as a function of the IR filling factor. For $IR_{\rm ff} = 10\%$ or above the IR pumping boosts the HCN excitation such that the HCN(5–4) flux density is in agreement with the observations. *Right*: HCN excitation model for the two-component dust/CO model for APM 08279+5255. The dashed line represents the "warm" gas with and IR illumination factor of unity, the dotted lines the "cold", dense gas with pure collisional excitation ($IR_{\rm ff} = 0$) and with an IR illumination of 0.25%. The solid line the sum of both IR illuminated components. The IR radiation temperature for both components is 220 K.

Figure 10 (left) exemplifies the variations of the HCN line SED as a function of the IR radiation temperature. We find that for dust temperatures below 100 K the excitation through vibrational pumping is small compared to the collisional excitation for H_2 densities typical for HCN emitting regions (∼10^{4-5} cm^{-3}). This is in line with the finding that IR pumping is not an important mechanism for local IR bright galaxies and most high-z sources as their dust SEDs show a much smaller contribution of dust with temperatures in excess of ∼50 K compared to APM 08279 (e.g. Lisenfeld et al. 2000, Beelen et al. 2006). For increasing dust temperatures, however, the IR pumping becomes very efficient. At a dust temperature of about 200 K the HCN excitation is completely dominated by IR pumping as long as the IR delution factor is above a few percent.

In Fig. 10 (middle) we show the effect of the IR dust field on the HCN excitation for the 1-component CO model ($T_{\rm IR} = 210$ K, $n(H_2) = 10^{4.2}$ cm^{-3}, $T_{\rm kin} = 220$ K, $r_0 = 790$ pc). For this model the collisional excitation of the HCN(5–4) line is negligible. But already an IR delution factor of ∼5% boosts the HCN luminosity by almost 2 orders of magnitude. For a filling factor of 10% or higher the IR pumping is strong enough to explain the observed HCN(5–4) luminosity in APM 08279. Thus the exceptional high dust temperature in APM 08279 provides a straightforward explanation for the strong HCN luminosity in this source without any ad hoc changes of the HCN abundance or extreme H_2 densities. This most likely also holds for the HCO^+ emission recently detected in APM 08279 (see Garcia-Burillo et al. 2006 and there discussion on the IR pumping of HCO^+).

Although the single component model with IR pumping yields a good fit to the CO and HCN line intensities as well as to the dust continuum it is presumably too simple as the HCN emission is known to arise from cloud cores with are typically an order of magnitude denser than those traced by the bulk of the CO emission. We therefore also show the effect of IR pumping for the 2-component CO model (Fig. 10, right). Since the IR filling factors for both components can not be derived from the available data, we consider here only the extreme case where the IR filling factor for the warm component, which is responsible for the dust emission at 220 K, is unity. From the Figure it can be seen that the IR pumping of the warm component, even in this extreme case, is not sufficient to explain the observed HCN(5–4) luminosity. Its contribution to the HCN(5–4) flux is similar to that of the pure collisional excitation from the cold dense medium. But even the sum of both mechanisms still underpredicts the HCN(5–4) luminosity so that also a small part of the cold dense gas needs to be exposed to the 220 K dust field. The required IR filling factor for the cold dense gas, however, is only 0.25%. The HCN(1–0) line luminosity from this model is dominated by the emission from the cold, dense gas and yields $L'_{\rm HCN} \approx 5 \times 10^{10}$ K km s^{-1} pc^2. The contribution due to collisional excitation is $L'_{\rm HCN} \approx 2 \times 10^{10}$ K km s^{-1} pc^2. We note that the IR filling factor for the cold gas remains low even if the IR filling for the warm gas is smaller than unity. That is, in the absence of the warm gas component the IR filling for the cold gas required to match the observed HCN(5–4) luminosity is still below 1%.

3.4. Magnification and size of the molecular gas distribution

In the following we use our effective (magnified) radius r_0 derived from the LVG and dust models in combination with the radial dependence of the magnification from the lens model of Egami et al. (2000, Fig. 9) to re-estimate the magnification and intrinsic size of the CO and dust emission regions. By definition, the apparent CO luminosity, $L'_{\rm CO}$, is related to the effective radius r_0 by

$$L'_{\rm CO} = T_{\rm b}\,\Delta V\,\pi\,r_0^2, \tag{9}$$

where $T_{\rm b}$ is the brightness temperature of the CO line and ΔV the observed line width. For a face–on, filled and isothermal disk we can express the radial dependence of the integrated CO luminosity in the case of radial differential magnification by

$$L'_{\rm CO}(r) = T_{\rm b}\,\Delta V\,2\pi \int_0^r m(r')\,r'\,{\rm d}r'. \tag{10}$$

Substituting $T_{\rm b}\,\Delta V$ by the observed CO luminosity and its equivalent radius and taking into account that the CO can not survive

closer to the central black hole than a minimum radius, $r_{\rm min}$, thus allows us to express $L'_{\rm CO}$ as a function of the intrinsic radius via

$$L'_{\rm CO}(r) = \frac{L'_{\rm CO\,obs}}{\pi r_0^2}\, 2\pi \int_{r_{\rm min}}^{r} m(r')\, r'\, {\rm d}r'. \quad (11)$$

In the following we assume $r_{\rm min} = 1$ pc which corresponds to the radius where the temperature for gas heated by the AGN with an intrinsic luminosity of $L_{\rm bol} = 5 \times 10^{13}\, L_\odot$ (Egami et al. 2000) has dropped below the dust sublimation temperature of ~1500 K. We can now compare the radial dependence of the $L'_{\rm CO}$ to the observed CO luminosity to derive the true source radius $r_{\rm true}$. The effective magnification can then be calculated via

$$m_{\rm eff} = \frac{r_0^2}{r_{\rm true}^2 - r_{\rm min}^2}. \quad (12)$$

We note that the above approach assumes that the caustic of the gravitational lens is roughly centered on the AGN and that we indeed trace gas circulating the AGN. This approximation is justified as the observed line width of 480 km s^{-1} is most likely dominated by the rotation of the molecular gas and the symmetry of the line profile suggests that the velocity profile is not differentially magnified. The radial dependence of $L'_{\rm CO}$ for this simple geometry is shown for selected LVG models in Fig. 11 (top). The intersection of these curves with the total observed CO luminosity and the relative contribution from the warm and cold gas component derived in Sect. 3.2.3 corresponds to the true source radius. For example, for an equivalent (magnified) source size of $r_0 = 1150$ pc (from our 2-component CO and dust models, for a random mixture of warm and cold gas), the intersection is at $r_{\rm true} = 105$ pc with an effective magnification of $m_{\rm eff} = 120$ – the same as the optical/IR magnification. We also obtain similar magnifications and source radii if we assume both components are spatially separated, with the hotter gas closer to the AGN. With $r_0 = 595$ pc for the warm gas, we get $r_{\rm true} = 60$ pc and $m_{\rm eff} = 95$. For the cold gas with $r_0 = 995$ pc and taking $r_{\rm min,cold} = 50$ pc we get $r_{\rm true} = 105$ pc and $m_{\rm eff} = 115$.

The true source radii, however, will be larger if the CO disk is inclined and the gas area filling factor is smaller than unity. For this more realistic geometry Eq. (11) becomes

$$L'_{\rm CO}(r) = \frac{L'_{\rm CO\,obs}}{\pi\, r_0^2}\, f_{\rm A} \int_{r_{\rm min}}^{r} \phi(r')\, m(r')\, r'\, {\rm d}r' \quad (13)$$

where $f_{\rm A}$ is the area filling factor of the CO emitting gas and $\phi(r')$ denotes the arc length of the intersection between a circle of constant magnification and the projected inclined disk:

$$\begin{aligned} \phi(r') &= 2\pi \quad \text{for } r' \le r_{\rm true}\cos(i) \\ \phi(r') &= 2\pi \arcsin\left(\frac{r_{\rm true}}{r'}\sqrt{\frac{r_{\rm true}^2 - r'^2}{r_{\rm true}^2 - r_{\rm true}^2\cos^2(i)}}\right) \\ &\qquad \text{for } r_{\rm true}\cos(i) < r' \le r_{\rm true} \\ \phi(r') &= 0 \quad \text{for } r' \ge r_{\rm true}. \end{aligned} \quad (14)$$

The effective magnification is then given by

$$m_{\rm eff} = \frac{r_0^2}{f_{\rm A}\cos(i)\,(r_{\rm true}^2 - r_{\rm min}^2)}. \quad (15)$$

As second case we show source radii and magnifications for an inclination of $i = 70°$ and a gas area filling factor of $f_{\rm A} = 0.5$ in Fig. 11 (bottom). For the filling factor we use here J1148+5251 at $z = 6.4$ as a template since it is the only high-z source for which multiple CO transitions as well as spatially resolved CO maps exist in literature (Bertoldi et al. 2003; Walter et al. 2003, 2004) which allow to estimate the gas filling factor. In this geometry the true source radius for the mixed model ($r_0 = 1150$ pc) is $r_{\rm true} = 275$ pc with an effective magnification of $m_{\rm eff} = 100$. For the spatially separated warm and cold gas models the corresponding radii and magnifications are $r_{\rm true} = 135$ pc with $m_{\rm eff} = 105$ (warm gas, $r_0 = 575$ pc, $r_{\rm min} = 1$ pc) and $r_{\rm true} = 325$ pc with $m_{\rm eff} = 60$ (cold gas, $r_0 = 995$ pc, $r_{\rm min} = 100$ pc).

Hence the true source size, which dominates the observed continuum and line emission, is very compact with $r_{\rm true} = 100{-}350$ pc and has a large effective magnification of $m_{\rm eff} = 60{-}110$ for a large range of geometries. A caveat is the unknown structure of the underlying CO distribution (expressed above as the filling factor of the CO emitting gas and the inclination). An arbitrary CO distribution with a low area filling factor could

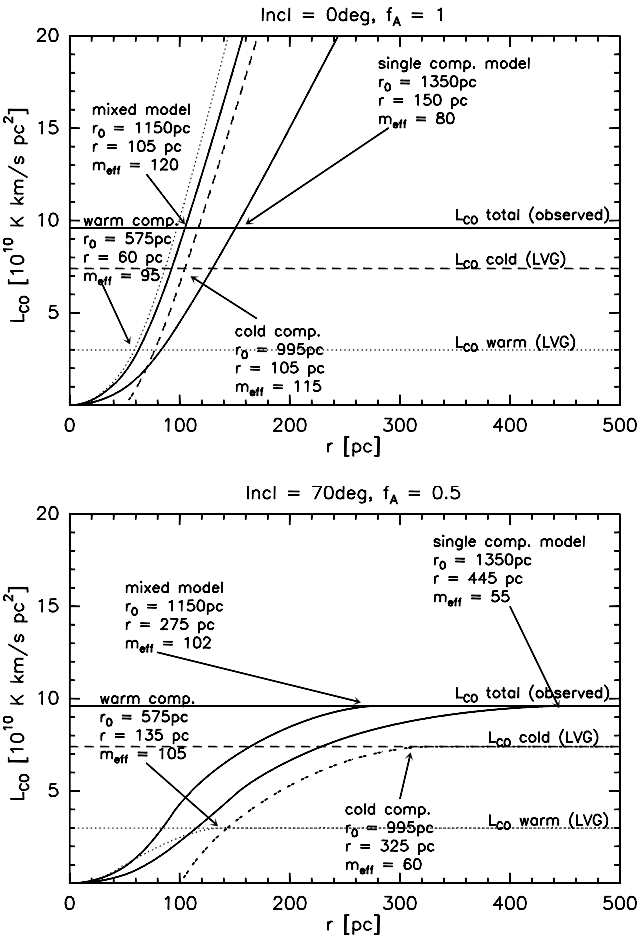

Fig. 11. Radial dependence of $L'_{\rm CO}$ calculated using the differential triple-image lens model from Egami et al. (2000, their Fig. 9) for a filled, face-on disk (top) and a disk seen at an inclination of 70° with an area filling factor for the CO emission of $f_{\rm A} = 0.5$ (bottom). Curves are shown for selected LVG models. For the cold component $r_{\rm min}$ has been set based on the radius of the warm component to 50 and 100 pc for the face-on and inclined case respectively. For all other models we used $r_{\rm min} = 1$ pc. The horizontal lines show the total, observed CO(1–0) line luminosity (Riechers et al. 2006, solid line) and the contributions to $L'_{\rm CO}$ from the cold (dashed line) and the warm (dotted line) gas components derived in Sect. 3.2.3. The relevant intersections between these curves are marked by the arrows for the four models. Resulting source radii and effective magnifications are given in the plot.

Table 3. Summary of best-fit model.

Parameter	Symbol in text	Unit	"Cold"	"Warm"	Remark
Apparent (Lensed) properties:					
Lens magnification	m	–	60−110	∼100	model from Egami et al. (2000)
Effective magnified radius	r_0	pc	995	575	
CO Luminosity	$m\,L'_{\rm CO(1-0)}$	K km s^{-1} pc^2	7.4×10^{10}	3.0×10^{10}	
FIR luminosity	$m\,L_{\rm FIR}$	$L_\odot$	2×10^{13}	1.7×10^{14}	
Apparent dust mass	$m\,M_{\rm d}$	$M_\odot$	2.6×10^{9}	2×10^{8}	
$M_{\rm gas}$ from CO	$m\,M(H_2{+}He)$	$M_\odot$	3.7×10^{11}	2.4×10^{10}	
$M_{\rm gas}$ from HCN	$m\,M(H_2{+}He)$	$M_\odot$	2×10^{11}	—	contribution from collisional excitation only
$M_{\rm gas}$ from dust	$m\,M(H_2{+}He)$	$M_\odot$	3.9×10^{11}	3×10^{10}	
$M_{\rm gas}$ from lvg model	$m\,M(H_2{+}He)$	$M_\odot$	4×10^{11}	1.3×10^{10}	
Intrinsic CO properties:					
Gas kinetic temperature	$T_{\rm kin}$	K	65	220	
Gas density	$n(H_2)$	cm^{-3}	1×10^{5}	1×10^{4}	
CO(1–0) brightness temp.	$T_{\rm b}$	K	50	60	
True CO luminosity	$L'_{\rm CO}$	K km s^{-1} pc^2	9.2×10^{8}	1.3×10^{8}	CO(1–0); $m_{\rm cold}=80$, $m_{\rm warm}$=100
Gas mass	$M(H_2{+}He)$	$M_\odot$	5×10^{9}	1×10^{8}	$m_{\rm cold}=80$, $m_{\rm warm}=100$
True CO radius	$r_{\rm true}$	pc	100−350	65−150	
Dynamical mass within r	$rV^2_{\rm rot}/G$	$M_\odot$	1.6×10^{10}	6.5×10^{9}	for $i=65°$, $r_{\rm cold}=250$ pc, $r_{\rm warm}=100$ pc
Intrinsic Dust quantities:					
Dust Temperature	$T_{\rm d}$	K	65 ± 18	220 ± 30	
True FIR Luminosity	$L_{\rm FIR}$	$L_\odot$	2.5×10^{11}	1.7×10^{12}	$m_{\rm cold}=80$, $m_{\rm warm}=100$
True dust mass	$M_{\rm d}$	$M_\odot$	3.3×10^{7}	2.1×10^{6}	$m_{\rm cold}=80$, $m_{\rm warm}=100$

extend well beyond the strongly magnified region. Thus the above estimates do not rule out that the compact, strongly magnified source is surrounded by additional, unlensed gas at larger radii. E.g. a molecular reservoir similar to that seen around M 82's starburst disk (Walter et al. 2002) or the spiral arms surrounding the nucleus of NGC 1068 (e.g. Schinnerer et al. 2000) would remain undetected as its contribution to the observed CO line intensities would be negligible. We note, however, that our analysis excludes an additional gas reservoir of several kpc size (as proposed by Papadopoulos et al. 2001) as it would have a significant contribution to the low-J CO lines (see also Riechers et al. 2006).

At a true radius of ∼100−250 pc, the lens image in the Egami et al. model is an Einstein ring or filled circle, which may explain the observed symmetric CO(9–8) distribution. Egami et al. predict a diameter $d \approx 0.5''$ for this ring – somewhat smaller than that derived from the CO(9–8) u,v fits. Thus our high resolution data also hint to a overall CO size out to ≈300 pc. A possible contradiction to this prediction is the morphology of the CO(1–0) distribution observed by Lewis et al. (2002a), which is an incomplete ring. New high-resolution VLA CO(1–0) observations with better signal-to-noise ratio, however, show that the CO is very similar to the IR distribution (Riechers et al. in prep.), supporting the idea that the CO magnification is higher than the values derived in other studies. The results of the 2-component modeling for CO, HCN, and the dust continuum are summarized in Table 3 and in the schematic diagram in Fig. 12.

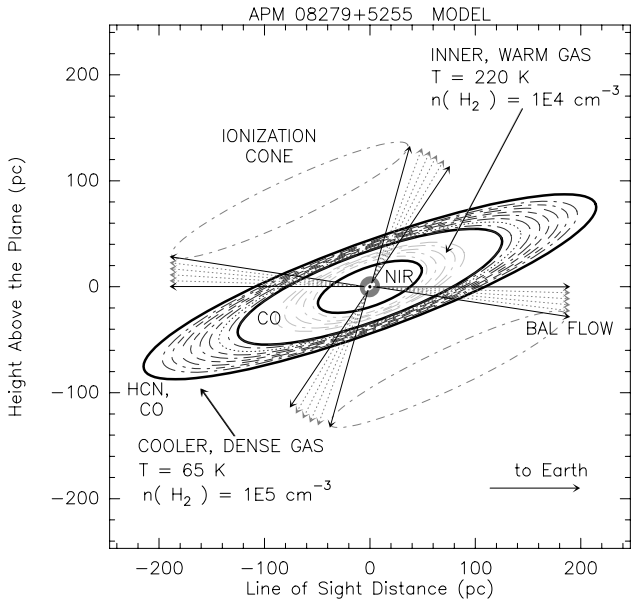

Fig. 12. Schematic diagram of our 2-component model for the CO, HCN, and mm-FIR dust emission from APM 08279+5255. There are two constraints on the geometry: 1) the large CO and HCN linewidths of 480 km s^{-1} imply the molecular rings are being viewed at high inclination. 2) Our line of sight to the black hole must intersect the BAL outflow cone, as in the model by Elvis (2000), so that UV broad absorption lines are seen against the UV continuum and UV emission lines of the accretion disk. In the molecular rings, the HCN and high-J CO lines mainly come from the "cold", dense component at >100 pc (outer disk), and some of the mid-J CO emission comes from the "warm", lower-density component at 50–100 pc (inner disk). The NIR radiation (Egami et al. 2000; Soifer et al. 2004) comes from the 1500 K-dust sublimation radius at ∼1 pc. The absorbers responsible for the X-ray BALs are located at radii of <0.1 pc from the black hole (Chartas et al. 2002; Hasinger et al. 2002).

4. Discussion

4.1. Heating of the molecular gas

The properties of the "warm" gas component are best explained by gas heated by the AGN itself. For an intrinsic luminosity of $L_{\rm bol} = 5\times10^{13}\,L_\odot$ the expected distance from the AGN for

dust at ∼200 K is ∼40 pc which is consistent within the uncertainties of the gas geometry with the average distance of the warm component derived above ($r_{\rm min} \approx 1$ pc, $r_{\rm max} \approx 60-130$ pc). This view is also supported by the dust spectrum which has the typical signature of a hot AGN torus (no PAH features, Soifer et al. 2004). At distances out to ∼350 pc the heating of the AGN has dropped to ∼65 K. This temperature has to be regarded as an upper limit as we here ignore the effect of self-screening in the molecular toroid. Without more detailed models on the dust heating from the AGN we can not rule out that also the "cold" gas component could be substantially heated by the AGN. We can, however, get an independent estimate on the heating source for the cold gas using our HCN analysis and the $L_{\rm IR}$–$L'_{\rm HCN}$ relation observed in local galaxies (Gao & Solomon 2004; recalculated to FIR-HCN by Carilli et al. 2005). From the HCN models the HCN(1–0) luminosity is $L'_{\rm HCN} = 5 \times 10^{10}\, m^{-1}$ K km s^{-1} pc^2 out of which $L'_{\rm HCN} = 2 \times 10^{10}\, m^{-1}$ K km s^{-1} pc^2 are due to collisional excitation. The later value corresponds to a FIR luminosity of $1.6 \times 10^{13}\, m^{-1}\, L_\odot$ which is close to the FIR luminosity derived for the cold gas component from the two component dust fit ($2 \times 10^{13}\, m^{-1}\, L_\odot$). Therefore the heating of the "cold" gas is probably dominated by star formation. Taking the magnification of the gas into account ($m_{\rm cold} \approx 80$) the implied star formation rate in the cold gas component is only $\sim 25\, M_\odot$ yr^{-1}. From our decomposition of the dust SED and the above arguments it is therefore clear that the FIR luminosity in APM 08279 is mainly powered by the AGN and that the contribution of active star formation to the total observed $L_{\rm FIR}$ is only of order ∼10%.

The radial temperature profile expected from the AGN heating also implies that it is unlikely that the cold and the warm gas are randomly mixed but it supports the interpretation that the cold gas arises from regions at larger distances from the AGN. As the cold gas dominates the HCN(5–4) line luminosity this is also supported by the somewhat narrower linewidth observed in the HCN(5–4) line. Further support for this picture comes from the analysis of the IR pumping of HCN which shows that the cold gas is only weakly exposed to the 220 K IR dust field ($\rm IR_{ff} < 1\%$). Such a low filling factor of the IR field contradicts the view that the cold gas is embedded in the warm gas phase.

4.2. Estimates of the molecular gas mass

We now establish estimates of the molecular gas mass using the CO, HCN and dust emission. For this we adopt the CO(1–0) and HCN(1–0) line luminosities derived in Sects. 3.2.3 and 3.3.2: $L'_{\rm CO}$(cold) = 7.4×10^{10} K km s^{-1} pc^2, $L'_{\rm CO}$(warm) = 3.0×10^{10} K km s^{-1} pc^2 and $L'_{\rm HCN} = 2 \times 10^{10}$ K km s^{-1} pc^2.

For high-z objects with high FIR luminosities, a ULIRG conversion factor of $0.8\, M_\odot$(K km s^{-1} pc^2)$^{-1}$ (Downes & Solomon 1998) is typically adopted to convert the lower-J CO line luminosities to the total molecular gas mass (see e.g. Solomon & Vanden Bout 2005). The original argument for using this factor is that much of the CO emission in the rapidly-rotating circumnuclear disks of ULIRGs comes from a spread-out intercloud medium, not from self-gravitating clouds (Downes et al. 1993). As we have seen from our two component gas model, even the warm component has a H_2 density typical for star forming galaxies ($n(H_2) \approx 10^4$ cm^{-3}) and about 70% of the CO(1–0) emission comes from extremely dense gas. Unlike typical CO lines from ULIRGS, the global CO emission in APM 08279 is therefore not dominated by a diffuse intercloud medium, but by very dense gas, with $n(H_2) = 10^5$ cm^{-3}. The conversion factor α scales as $n^{0.5}/T_{\rm b}$, both for self-gravitating molecular clouds (see the typical ranges of the factor α listed by Radford et al. (1991), and for a more distributed medium that is not self-gravitating (Downes et al. 1993). For the cold gas component of APM 08279, the CO brightness temperatures is similar to those in ULIRGS ($T_{\rm b} \approx 50$ K), but the *gas density* is about forty times higher than in ULIRGS. This suggests the conversion factor should be $\alpha \approx (40)^{0.5} \times 0.8 \approx 6\, M_\odot$(K km s^{-1} pc^2)$^{-1}$. This gives us a first estimate of the molecular gas mass, based on CO alone:

(1) From the CO luminosity of the cold gas component and the "scaled ULIRG factor" of $5\, M_\odot$(K km s^{-1} pc^2)$^{-1}$ we obtain $M_{\rm cold} = 3.7 \times 10^{11}\, m^{-1}\, M_\odot$. Using the standard ULIRG factor for the warmer gas adds only $2.4 \times 10^{10}\, m^{-1}\, M_\odot$. gas mass leading to $M_{\rm total} = 3.9 \times 10^{11}\, m^{-1}\, M_\odot$. This gas mass should be compared to estimates from HCN and from the dust:

(2) For the HCN(1–0) line luminosity, Gao & Solomon (2004) suggest a conversion factor of $\sim 10\, M_\odot$(K km s^{-1} pc^2)$^{-1}$. This yields a value of $M_{\rm cold} = 2 \times 10^{11}\, m^{-1}\, M_\odot$.

(3) From our dust models we derive a dust mass of the cold component of $2.6 \times 10^9\, m^{-1}\, M_\odot$. If we multiply this dust mass by a gas-to-dust mass ratio of 150, we obtain a gas mass of $M_{\rm cold} = 3.9 \times 10^{11}\, m^{-1}\, M_\odot$, the same as the estimate from the CO but a factor of two higher than the estimate from HCN. With the same gas-to-dust mass ratio the warm dust only adds $M_{\rm warm} = 3 \times 10^{10}\, m^{-1}\, M_\odot$ leading to $M_{\rm total} = 4.2 \times 10^{11}\, m^{-1}\, M_\odot$. The mass estimate from the dust could be lower, if metals have been enriched to a value 2 to 5 times solar, as suggested by X-ray observations of the iron K-shell absorption edge in APM 08279 (Hasinger et al. 2002).
If, however, we accept the mass estimate from the optically thin part of the dust spectrum as a good working estimate, we can compare this mass directly with the CO and HCN luminosities, to "derive" the conversion factor α for the cold dense gas. This directly gives $\alpha_{\rm CO} = 5.2\, M_\odot$ (K km s^{-1} pc^2)$^{-1}$ and $\alpha_{\rm HCN} = 20\, M_\odot$ (K km s^{-1} pc^2)$^{-1}$. $\alpha_{\rm CO}$ agrees well with our value estimated by scaling the ULIRG factor. The conversion factor for HCN is a factor of 2 higher than the values given in Gao & Solomon (2004) by in agreement for those derived in Arp 220 and NGC 6240 (Greve et al. 2006).

(4) We can also estimate the gas mass from the LVG models rather than using a conversion factor (see Eq. (8)). Assuming that the low [CO]/(dv/dr) we use in our models is mainly due to a higher turbulence and not due to a lower CO abundance, (dv/dr) is ∼5 km s^{-1} pc^{-1}. For the turbulence line width we adopt here $\Delta V_{\rm turb} = 100$ km s^{-1} based on estimates for SMM J02399-0136 ($z = 2.8$) where the ratio of the local velocity dispersion to rotation velocity has been determined to be ∼0.2 (Genzel et al. 2003). Similar turbulence motions have been derived for Arp 220 (Downes & Solomon 1998). With this number the gas mass from the LVG model becomes $M_{\rm cold} = 4 \times 10^{11}\, m^{-1}\, M_\odot$ and $M_{\rm warm} = 1.3 \times 10^{10}\, m^{-1}\, M_\odot$ in agreement with the estimates above. With these numbers the equivalent path length $\Delta V/({\rm d}v/{\rm d}r)$ through the molecular disk is ∼20 pc.

(5) Another check on the minimum gas mass is to simply calculate the CO optically thin limit. Following Solomon et al. (1997), this is

$$M_{\rm thin}({\rm H_2 + He}) = 9.4 \times 10^{-3} L'_{\rm CO} T_{\rm ex}, \qquad (16)$$

where $L'_{\rm CO}$ is the CO(1–0) line luminosity in K km s^{-1} pc^2, $T_{\rm ex}$ is the excitation temperature in K, $M_{\rm thin}$ is a lower limit to the gas mass in $M_\odot$, and the numerical coefficient is for an

assumed (Milky Way) CO abundance of [CO]/[H_2] of 10^{-4}. Thus for the cold molecular gas in APM 08279 with a CO abundance of 5×10^{-5} the lower limit to the gas mass is $M_{\rm thin} = 5.2 \times 10^{10}\, m^{-1}\, M_\odot$.

In summary, the gas mass estimates from the CO, HCN, the optically-thin millimeter dust continuum, and the CO radiative-transfer modeling are all in reasonable agreement and lead to a total gas mass of $M_{\rm total} = 4 \times 10^{11}\, m^{-1}\, M_\odot$. The gas mass is dominated by the cold dense HCN emitting gas. Taking the magnification of $m_{\rm cold} \approx 80$ into account the intrinsic gas mass of APM 08279 is $\sim 5 \times 10^9\, M_\odot$. The implied CO luminosity-to-gas mass conversion factor is about 5 to 6 $M_\odot$ (K km s^{-1} pc^2)$^{-1}$.

4.3. Mass budget in the central region of APM 08279

Having established estimates for the intrinsic size of the CO emitting region (Sect. 3.4) and for the molecular gas mass (Sect. 4.2) we now discuss the mass budget in the central region of APM 08279 to test if it falls on the $M_{\rm BH} - \sigma_*$ relation found for local galaxies (Gebhardt et al. 2000; Ferrarese & Merritt 2000). Shields et al. (2006) have recently addressed this question for a sample of high-z QSOs, including APM 08279. For APM 08279 those authors assume a much lower magnification (7) than we do (∼100), and consequently assume the CO is spread out over a 2-kpc diameter. In the present paper, we concentrate the discussion toward the central few hundred-pc region:

The bolometric luminosity of the quasar, after correcting for the factor-of-100 amplification by gravitational lensing, is still an enormous $7 \times 10^{13}\, L_\odot$. From the argument originally due to Zel'dovich & Novikov (1964), the lower limit to the black hole mass, if electron scattering produces the main opacity, is

$$M_{\rm BH} \geq 3.0 \times 10^{-5}\, L_{\rm bol}, \qquad (17)$$

with $M_{\rm BH}$ and $L_{\rm bol}$ in solar units. This means the mass of the black hole at the center of APM 08279 likely exceeds $2 \times 10^9\, M_\odot$. If the local $M_{\rm BH} - \sigma_*$ relation were to hold, then the stellar bulge would have a mass of $M_{\rm bulge} = 1.4 \times 10^{12}\, M_\odot$. To estimate the stellar mass in the central few hundred pc, we assume a central density profile for the bulge of $\rho \sim r^{-2}$ (Jaffe 1983; Tremaine et al. 1994) and a bulge scale length of 5 and 10 kpc. Since the inclination of the molecular disk is largely unconstrained, we treat it in the following as a free parameter. Using Eq. (13), we have first calculated the CO source size as function of the inclination. We use here as an example only the dense cold gas component from the two component model, since the warm gas does not contribute significantly to the mass. We have further used a gas filling factor of unity and $r_{\rm min} = 1$ pc, since then the CO source is most compact, which maximizes its gravitational impact in the central region. From the CO source size we have then calculated the dynamical mass and the stellar mass contribution. The resulting mass contributions as a function of the inclination are shown in Fig. 13. From this figure it is obvious that, independent of the inclination, the sum of the black hole and the gas mass is always lower than the dynamical mass. Given that we show a model with one of the highest central gas mass concentration, this holds for all other configurations of the two component gas model as well. The figure also shows that the stellar mass exceeds the dynamical mass for inclinations larger than ∼40°. Note that the inclination for which the stellar and the dynamical mass intersect is independent of the assumed gas model since both masses scale linear with the underlying source radius (which is determined by the gas model). Taking the gas and black hole mass into account, the limits for the inclination of the CO disk become <25° and <35° for a bulge scale length of 5 and 10 kpc respectively. Thus, if the local $M_{\rm BH} - \sigma_*$ relation were to hold, the implied intrinsic rotation velocity of the CO disk would be $v_{\rm rot} > 900$ km s^{-1}, and $v_{\rm rot} > 1200$ km s^{-1}. Given that the observed CO linewidth of 480 km s^{-1} is already one of the highest linewidths observed in local and high-z QSOs (see e.g. Solomon & Vanden Bout 2005 and references therein), it is more likely that we see the CO disk in APM 08279 at high inclination, which implies that $M_{\rm BH} - \sigma_*$ does not hold for APM 08279.

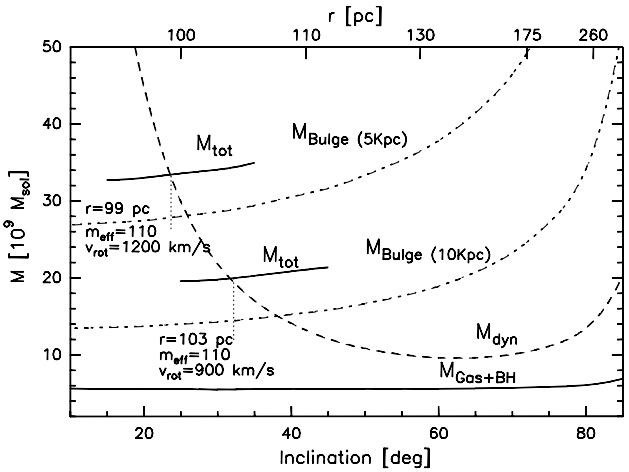

Fig. 13. Black hole, molecular, stellar and dynamical mass in the central region of APM 08279 as a function of assumed inclination of the molecular disk. Radii as a function of the inclination have been calculated from Eq. (13) for the cold, dense gas ($r_0 = 995$ pc, $r_{\rm min} = 1$ pc) using a filling factor of unity. The stellar mass has been calculated using a scalelength of the stellar bulge of 5 and 10 kpc and assuming the $M_{\rm BH} - \sigma_*$ relation were to hold. Variations of the stellar bulge contribution with inclination are only due to changes of the size of the region considered. The corresponding radii are given at the top axis of the plot. The inclination for which the total mass (gas + stellar + BH) matches the dynamical mass are given for both bulge geometries together with the corresponding numbers for the true CO radius, effective magnification of the molecular gas, and the CO rotation velocity.

The conclusion is that for this QSO at $z = 3.9$, the supermassive black hole is already in place, but the assembly of the stellar bulge is still in progress. Similar conclusions have been gained by Walter et al. (2004) for J1148+5251 at $z = 6.4$ and by Shields et al. (2006) on a larger sample of high-z QSOs. A caveat arising from the special lens configuration in APM 08279 is, that the emission lines only trace a very compact region surrounding the AGN which implies that this conclusion only holds if the central density profile of the stellar bulge follows a $\rho \sim r^{-2}$ profile to the central ∼100 pc.

4.4. Comparison with other high-z QSOs

Our observations show that the CO line SED of APM 08279 is strikingly different from those of other high-z QSOs and nearby starburst galaxies (Fig. 14). The turnover of the CO SED in high-z QSOs typically occurs at the CO(6–5) or CO(7–6) transition (e.g. BR1202-0725, J1148+5251). This also holds for the F10214 the Cloverleaf and other high-z QSOs (Weiß et al. in prep). In contrast to these sources, the CO line SED turnover in APM 08279 occurs at the CO(10–9) line! This is mainly due to the high H_2 density in excess of 10^5 cm^{-3} which is more than ten times higher than those in other dusty QSOs. This probably also explains the high luminosity of the HCN line in APM 08279, relative to that in other quasars. The presence of a high-temperature

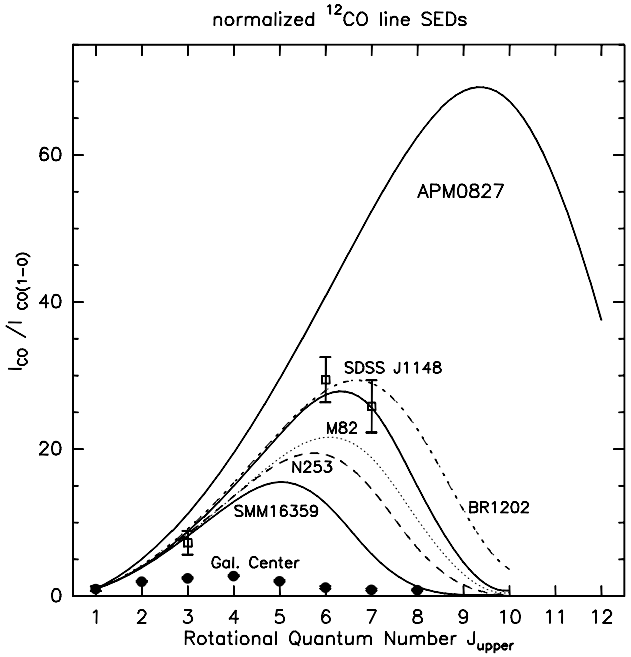

Fig. 14. Comparison of the CO line SEDs of selected local and high-z galaxies. The SEDs are shown for APM 08279 (this paper, Fig. 7), BR1202-0725 ($z = 4.7$, Carilli et al. 2002; Riechers et al. 2006), J1148+5251 ($z = 6.4$, open squares, Bertoldi et al. 2003; Walter et al. 2003) the high-excitation component in the center of M82 (Weiß et al. 2005b), NGC 253 center (Güsten et al. 2006) SMM 16359 ($z = 2.5$, Weiß et al. 2005a) and the Galactic Center (solid circles, Fixsen et al. 1999). The CO line SEDs are normalized by their CO(1–0) flux density.

(200 K) CO and dust component also distinguishes APM 08279 from other high-z quasars detected in CO so far. From the lens modeling, both the cold component, and the warm molecular gas component in APM 08279 appear to be closer to the nucleus than in the other quasars which makes it likely that the 200 K component is heated directly by the AGN. As noted by Blain (1999), part of these differences relative to other quasars may be due to the configuration of the gravitational lens, which gives us a high-magnification zoom right into the central 100–300 pc radius of APM 08279. If such an inner circumnuclear region of high-density molecular gas exists in all the high-z quasars detected in molecular lines so far, then it might be relatively inconspicuous, because it is not highly magnified, and it has a low filling factor relative to the greater circumnuclear region out to a radius of 1 kpc. Conversely, in APM 08279, we may be missing the gas out to 1 kpc, because the central region outshines the more extended gas due to its high flux amplification. Although the Egami et al. (2000) lensing model indicates the central region may be free of differential magnification, we still may not even see the outer 1 kpc-radius region, simply because its magnification has fallen by nearly a factor of 100.

5. Conclusions

We observed APM 08279 as part of our ongoing CO line SED study of high-z sources at the 30 m telescope. Besides the previously observed CO(4–3) and (9–8) lines, new detections included the CO(6–5), (10–9) and the (11–10) lines. We also present improved observations of the CO(4–3), CO(9–8), and HCN(5–4) lines and the 1.4 and 3 mm dust continuum with the IRAM Interferometer. The simple fact that such high CO lines are detected shows that the gas properties of APM 08279 differ greatly from those seen in other high-z QSOs and local starbursts.

The CO and dust size measurement, combined with the lensing model of Egami et al. (2000) shows that the source region is very compact (radius ~60–300 pc) and that its magnification is similar to the optical/IR magnification (~60−110). The high CO excitation and the dust continuum emission are best modeled with a 2-component gas model. The warm (~220 K) gas component is most likely directly heated by the AGN and arises from radii between 60–150 pc. This component dominates the FIR luminosity (~90%). The cooler gas (~65 K), which carries ~90% of the total gas mass of $M_{\rm gas} \approx 5 \times 10^9\,M_\odot$ arises from somewhat larger radii. Its main characteristic is a high H_2 density of $\sim 1{\times}10^5$ cm^{-3} – about 10 times higher than the gas in other high-z QSOs and local starburst galaxies. The high gas density implies that the standard ULIRG conversion factor, usually applied to high-z galaxies, does not provide a good estimate of the molecular gas in APM 08279. Our study suggests that conversion factor for CO, in this special case, is $\alpha_{\rm CO} \approx 5\,M_\odot\,({\rm K\ km\,s^{-1}\ pc^2})^{-1}$.

Although the gas density for the cold gas is typical for the HCN emitting volume in local ULIRGs it is not high enough to explain the observed HCN(5–4) luminosity in APM 08279. From LVG models including IR pumping via the 14 μm bending mode of HCN we conclude that the hot dust heated by the AGN efficiently boosts the HCN excitation and that this excitation channel is more important than the collisional excitation for this particular source. The star formation rate associated with the dense gas component is only $\sim 25\,M_\odot\,{\rm yr}^{-1}$.

An estimate of the mass budget in the central region of APM 08279 suggests that the black hole and gas mass does not leave sufficient room for a stellar mass contribution following the local $M_{\rm BH} - \sigma_*$ relation for reasonable inclinations of the molecular disk. Hence we conclude that the super-massive black hole in APM 08279 is already in place, before the buildup of the stellar bulge is complete.

Acknowledgements. We thank the IRAM receiver engineers D. John and S. Navarro for their great help in optimizing receiver tunings as well as the 30 m telescope operators and the Plateau de Bure Interferometer operators for their all-around assistance with the observing in general. IRAM is supported by INSU/CNRS (France), MPG (Germany) and IGN (Spain).

References

Aalto, S., Johansson, L. E. B., Booth, R. S., & Black, J. H. 1991, A&A, 249, 323
Barvainis, R., & Ivison, R. 2002, ApJ, 571, 712
Bayet, E., Gerin, M., Phillips, T. G., & Contursi, A. 2004, A&A, 427, 45
Beelen, A., Cox, P., Benford, D. J., et al. 2006, ApJ, 642, 694
Bertoldi, F., Carilli, C. L., Menten, K. M., et al. 2000, A&A, 360, 92
Bertoldi, F., Cox, P., Neri, R., et al. 2003, A&A, 409, L47
Blain, A. W. 1999, MNRAS, 304, 669
Blain, A. W., Smail, I., Ivison, R. J., Kneib, J. P., & Frayer, D. T. 2002, Phys. Rep., 369, 111
Blain, A. W., Barnard, V. E., & Chapman, S. C. 2003, MNRAS, 338, 733
Carilli, C. L., Kohno K., Kawabe, R., et al. 2002, AJ, 123, 1838
Carilli, C. L., Solomon, P. M., Vanden Bout, P., et al. 2005, ApJ, 618, 586
Carroll, T. J., & Goldsmith, P. F. 1981, ApJ, 245, 891
Chartas, G., Brandt, W. N., Gallagher, S. C., & Garmire, G. 2002, ApJ, 579, 169
Downes, D., & Solomon, P. M. 1998, ApJ, 507, 615
Downes, D., & Solomon, P. M. 2003, ApJ, 528, 37
Downes, D., Solomon, P. M., & Radford, S. J. E. 1993, ApJ, 414, L13
Downes, D., Solomon, P. M., & Radford, S. J. E. 1995, ApJ, 453, L65
Downes, D., Neri, R., Wiklind, T., Wilner, D. J., & Shaver, P. A. 1999, ApJ, 513, L1 (D99)
Egami, E., Neugebauer, G., Soifer, B. T., & Matthews, K. 2000, ApJ, 535, 561
Elvis, M. 2000, ApJ, 545, 63
Ferrarese, L, & Merritt, D. 2000, ApJ, 539, 9
Fixsen, D. J., Bennett, C. L., & Mather, J. C. 1999, ApJ, 526, 207
Flower, D. R. 2001, J. Phys. B: At. Mol. Opt. Phys., 34, 1

Gao, Y., & Solomon, P. M. 2004, ApJ, 606, 271
Garcia-Burillo, S., Gracia-Carpio, J., Guelin, M., et al. 2006, ApJ, 645, 17
Gebhardt, K., Bender, R., Bower, G., et al. 2000, ApJ, 539, 13
Genzel, R., Baker, A. J., Tacconi, L. J., et al. 2003, ApJ, 584, 633
Greve, T. R., Ivison, R. J., Bertoldi, F., et al. 2004, MNRAS, 354, 779
Greve, T. R., Bertoldi, F., Smail, I., et al. 2005, MNRAS, 359, 1165
Greve, T. R., Papadopoulos, P. P., Gao, Y., & Radford, S. J. E. 2006, ApJ, in press [arXiv:astro-ph/0610378]
Güsten, R., & Downes, D. 1980, A&A, 87, 6
Güsten, R., Phillip, S. D., Weiß, A., & Klein, B. 2006, A&A, 454, 115
Hasinger, G., Schartel, N., & Komossa, S. 2002, ApJ, 573, L77
Helfer, T., & Blitz, L. 1997, ApJ 478, 233
Helou, G., Soifer, B. T., & Rowan-Robinson, M. 1985, ApJ, 298, L7
Ibata, R. A., Lewis, G. F., Irwin, M. J., Lehár, J., & Totten, E. J. 1999, AJ, 118, 1922
Irwin M. J., Ibata R. A., Lewis G. F., & Totten E. J. 1998, ApJ, 505, 529
Ivison, R. J. 2006, MNRAS, 370, 495
Jaffe, W. 1983, MNRAS, 202, 995
Krügel, E., & Siebenmorgen, R. 1994, A&A 288, 929
Ledoux, C., Théodore, G., Petitjean, P. P., et al. 1998, A&A, 339, L77
Lepp, S., & Dalgarno, A. 1996, A&A, 306, L21
Lewis, G. F., Chapman, S. C., Ibata, R. A., Irwin, M. J., & Totten, E. J. 1998, ApJ, 505, L1
Lewis, G. F., Carilli, C., Papadopoulos, P., & Ivison, R. J. 2002a, MNRAS, 330, L15
Lewis, G. F., Ibata, R. A., Ellison, S. L., et al. 2002b, MNRAS, 334, L7
Lisenfeld, U., Isaak, K. G. & Hills, R. 2000, MNRAS, 312, 441
Papadopoulos, P., Ivison, R., Carilli, C., & Lewis, G. 2001, Nature 409, 58
Paglione, T. A. D., Jackson, J. M., & Ishizuki, S. 1997, ApJ, 484, 656
Paglione, T. A. D., Wall, W. F., Young, J. S., et al. 2001, ApJS, 135, 183
Priddey, R. S., & McMahon, R. G. 2001, MNRAS 324, 17
Radford, S. J. E., Solomon, P. M., & Downes, D. 1991, ApJ, 368, L15
Riechers, D. A., Walter, F., Carilli, C. L., et al. 2006, ApJ, 650, 604
Rowan-Robinson, M. 2000, MNRAS, 316, 885
Sakamoto, K., Ho, P. T. P., Iono, D., et al. 2006, ApJ, 636, 685
Schinnerer, E., Eckartk, A., Tacconi, L. J., Genzel, R., & Downes, D. 2000, ApJ 533, 850
Schoier, F. L., van der Tak, F. F. S., van Dishoeck, E. F., & Black, J. H. 2005, A&A 432, 369
Shields, G. A., Menezes, K. L., Massart, C. A., & Vanden Bout, P. 2006, ApJ, 641, 683
Scoville, N. Z., Yun, M. S., & Bryant, P. M. 1997, ApJ, 484, 702
Soifer, B. T., Charmandaris, B., Brandl, B. R., et al. 2004, ApJS, 154, 151
Solomon, P. M., & Vanden Bout, P. 2005, ARA&A, 43, 677
Solomon, P. M., Downes, D. & Radford, S. J. E. 1992, ApJ, 398, L29
Solomon, P. M., Downes, D., Radford, S. J. E., & Barrett, J. W. 1997, ApJ, 478, 144
Spergel, D. N., Verde, L., Peiris, H., et al. 2003, ApJS, 148, 175
Stark, A. A., Bally, J., Wilson, R. W., & Pound, M. W. 1989, in The Center of the Galaxy, IAU Symp. 135, ed. M. Morris (Dordrecht: Kluwer), 128
Stutzki, J., Genzel, R., Harris, A.I., Herman, J., & Jaffe, D.T. 1988, ApJ, 330, 125
Thorwirth, S., Wyrowski, F., Schilke, P., et al. 2003, ApJ, 586, 338
Tremaine, S., Richstone, D. O., Byun, Y.-I., et al. 1994, 107, 634
Usero, A., Garcia-Burillo, S., Fuente, A., Martin-Pintado, J., & Rodriguez-Fernandez, N. J. 2004, A&A, 419, 897
Vollmer, B., & Duschl, W. J. 2001, A&A, 377, 1016
Wagg, J., Wilner, D. J., Neri, R., Downes, D., & Wiklind, T. 2005, ApJ, 634, L13.
Walter, F., Weiß, A., & Scoville, N. 2002, ApJ, 580, 21
Walter, F., Bertoldi, F., Carilli, C. L., et al. 2003, Nature, 424, 406
Walter, F., Carilli, C., Bertoldi, F., et al. 2004, ApJ, 615, L17
Wang, M., Henkel, C., Chin, Y. N., et al. 2004, A&A, 422, 883
Weiß, A., Henkel, C., Downes, D. & Walter, F. 2003, A&A, 409, L41
Weiß, A., Downes, D. Walter, F., & Henkel, C. 2005a, A&A, 440, L45
Weiß, A., Walter, F. & Scoville, N. Z. 2005b, A&A, 438, 533
Zel'dovich, Y. B., & Novikov, I. D. 1964, Dokl. Akad. Nauk. SSR, 158, 811; english translation 1965 Sov. Phys. Dokl., 9, 834